

1 **NON-LOCAL KINETIC AND MACROSCOPIC MODELS FOR**
2 **SELF-ORGANISED ANIMAL AGGREGATIONS**

JOSÉ A. CARRILLO

Department of Mathematics, Imperial College London
London SW7 2AZ, United Kingdom

RALUCA EFTIMIE

Division of Mathematics, University of Dundee
Dundee, DD1 4HN, United Kingdom

FRANCA HOFFMANN

University of Cambridge, Centre for Mathematical Sciences
Wilberforce Road, Cambridge CB3 0WA, United Kingdom

(Communicated by the associate editor name)

ABSTRACT. The last two decades have seen a surge in kinetic and macroscopic models derived to investigate the multi-scale aspects of self-organised biological aggregations. Because the individual-level details incorporated into the kinetic models (e.g., individual speeds and turning rates) make them somewhat difficult to investigate, one is interested in transforming these models into simpler macroscopic models, by using various scaling techniques that are imposed by the biological assumptions of the models. However, not many studies investigate how the dynamics of the initial models are preserved via these scalings. Here, we consider two scaling approaches (parabolic and grazing collision limits) that can be used to reduce a class of non-local 1D and 2D models for biological aggregations to simpler models existent in the literature. Then, we investigate how some of the spatio-temporal patterns exhibited by the original kinetic models are preserved via these scalings. To this end, we focus on the parabolic scaling for non-local 1D models and apply asymptotic preserving numerical methods, which allow us to analyse changes in the patterns as the scaling coefficient ϵ is varied from $\epsilon = 1$ (for 1D transport models) to $\epsilon = 0$ (for 1D parabolic models). We show that some patterns (describing stationary aggregations) are preserved in the limit $\epsilon \rightarrow 0$, while other patterns (describing moving aggregations) are lost. To understand the loss of these patterns, we construct bifurcation diagrams.

3 **1. Introduction.** Over the past 10-20 years a multitude of kinetic and macroscopic
4 models have been introduced to investigate the formation and movement of various
5 biological aggregations: from cells [5, 1] and bacteria [56] to flocks of birds, schools
6 of fish and even human aggregations (see, for example, [60, 18, 55, 19, 29, 8, 25] and
7 the references therein). The use of kinetic or macroscopic approaches is generally
8 dictated by the problem under investigation: (i) kinetic (transport) models focus on

2010 *Mathematics Subject Classification.* Primary: 35L40, 35L65, 35K55, 92B99; Secondary: 82C40, 65M06,

Key words and phrases. self-organised aggregations; kinetic models; macroscopic models; non-local interactions; asymptotic preserving methods.

9 changes in the density distribution of individuals that have a certain spatial position,
 10 speed and movement direction (or are in some activity state [7]); (ii) macroscopic
 11 models focus on changes in the averaged total density of individuals [20, 31].

12 Generally, these kinetic and macroscopic models assume that individuals, parti-
 13 cles, or cells can organise themselves in the absence of a leader. The factors that
 14 lead to the formation of self-organised aggregations are the interactions among indi-
 15 viduals as a result of various social forces: repulsion from nearby neighbours, attrac-
 16 tion to far-away neighbours (or to roosting areas [23]) and alignment/orientation
 17 with neighbours positioned at intermediate distances. These interaction forces are
 18 usually assumed to act on different spatial ranges, depending on the communica-
 19 tion mechanisms used by individuals; e.g., via acoustic long-range signals, or via
 20 chemical/visual short-range signals. The non-locality of the attractive and align-
 21 ment/orientation interactions is supported by radar tracking observations of flocks
 22 of migratory birds, which can move with the same speed and in the same direction
 23 despite the fact that individuals are 200-300 meters apart from each other [48]. For
 24 the repulsive forces some models consider non-local effects generated by decaying
 25 interactions with neighbours positioned further and further away [32], while other
 26 models consider only local effects [59]. In the case of continuous mesoscopic and
 27 macroscopic models, the non-local interactions are modelled by interaction kernels
 28 (see Figure 1 for 2D and 1D kernels). The most common choices for these kernels
 29 are Morse potential-type kernels [20, 18, 19, 22] (see Figure 1(b)) and Gaussian
 30 kernels [33, 32, 31, 49] (see Figure 1(c)).

31 Due to their complex structure, kinetic models are difficult to investigate. Al-
 32 though progress has been made in recent years, mainly regarding the existence and
 33 stability of various types of solutions and the analytic asymptotic methods that al-
 34 low transitions from kinetic (mesoscopic) to macroscopic models (see, for example,
 35 [44, 54, 6, 18, 17, 29, 28, 11, 9, 41] and the references therein), it is still difficult
 36 to study **analytically and numerically** the spatial and spatio-temporal aggregation
 37 patterns exhibited by the kinetic models. For example, there are very few studies
 38 that investigate the types of spatiotemporal patterns obtained with 2D and 3D kin-
 39 etic models (see the review in [31]). Moreover, the presence of non-local interaction
 40 terms increases the complexity of the models, leading to a larger variety of patterns
 41 that are more difficult to be analysed. While numerical and analytical studies have
 42 been conducted to investigate the patterns in 1D non-local models [32, 34, 14], such
 43 an investigation is still difficult in the 2D non-local case (see [36]).

44 The first goal of this article is to start with a class of 1D and 2D non-local kinetic
 45 models for self-organised aggregations that incorporate all three social interactions,
 46 and to show, through different parabolic scaling approaches, that these models can
 47 be reduced to known non-local parabolic models for swarming; see Figure 2 for a
 48 diagram illustrating this approach. For the 1D case, similar analytical scalings have
 49 been done in the context of bacterial chemotaxis [58] and for the kinetic model (1)
 50 for individuals moving along a line [35].

51 **The next aim is to investigate the numerical preservation of patterns between the**
 52 **mesoscopic and macroscopic scales. We use asymptotic preserving numerical meth-**
 53 **ods [46, 47, 21, 24], to obtain a better understanding of what happens with the 1D**
 54 **patterns via the parabolic scaling. With the help of these methods, we investigate**
 55 **numerically the preservation of stationary aggregations (that arise via steady-state**
 56 **bifurcations) and moving aggregations (that arise via Hopf bifurcations), as the**
 57 **scaling parameter ε is varied from large positive values ($\varepsilon = 1$) corresponding to**

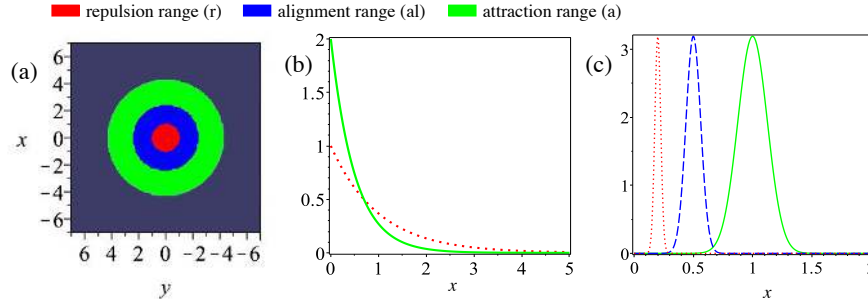


FIGURE 1. 2D and 1D spatial kernels for social interactions. (a) 2D: Attractive (K_a), repulsive (K_r) and alignment (K_{al}) kernels described by equation (21); (b) 1D: Morse-type kernels: $K_{r,a}(x) = e^{-|x|/s_{r,a}}$. (c) 1D: Translated Gaussian kernels K_j as defined in (3) with $j = r, al, a$.

58 the kinetic models to zero values corresponding to the limiting parabolic models.
 59 To visualise the transitions between different patterns as $\varepsilon \rightarrow 0$, we construct bi-
 60 furcation diagrams for the amplitude of the solutions. For the 2D kinetic models,
 61 we focus on two analytical scalings that lead to two different nonlocal parabolic
 62 models. Our final target is to show the reader that by considering such scaling
 63 approaches, we may lose certain aspects of the model dynamics - as emphasised by
 64 the numerical simulations in the 1D case.

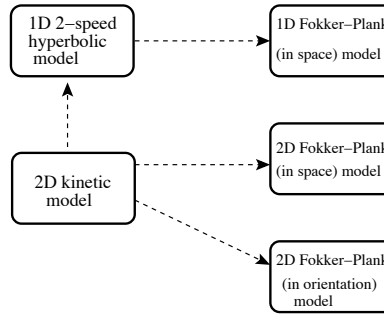


FIGURE 2. Schematic diagram of the scaling and reductionist approach taken here.

65 The article is structured as follows. Section 2 contains a detailed description of
 66 the 1D non-local models for animal aggregations, followed by the parabolic scaling
 67 of these models. We also investigate analytically the steady states of the kinetic and
 68 corresponding parabolic models. Section 3 contains a description of the 2D non-
 69 local models, followed by a parabolic limit and a “grazing collision” limit, which
 70 lead to different types of macroscopic models of parabolic type. Section 4 focuses
 71 on asymptotic preserving methods for 1D models, and shows the spatial and spatio-
 72 temporal patterns obtained with the parabolic and kinetic models, for some specific
 73 parameter values. Here, we come back to the steady states of the 1D kinetic and
 74 parabolic models, and investigate them numerically. We conclude in Section 5 with
 75 a summary and discussion of the results.

2. Description of 1D models. The following one-dimensional model was introduced in [33, 32] to describe the movement of the densities of left-moving (u^-) and right-moving (u^+) individuals that interact with conspecifics via social interactions:

$$\frac{\partial u^+}{\partial t} + \gamma \frac{\partial u^+}{\partial x} = -u^+ \lambda^+[u^+, u^-] + u^- \lambda^-[u^+, u^-], \quad (1a)$$

$$\frac{\partial u^-}{\partial t} - \gamma \frac{\partial u^-}{\partial x} = u^+ \lambda^+[u^+, u^-] - u^- \lambda^-[u^+, u^-], \quad (1b)$$

$$u^\pm(x, 0) = u_0^\pm(x). \quad (1c)$$

Here γ is the constant speed and λ^+ (λ^-) is the rate at which right-moving (left-moving) individuals turn left (right). **Since the rates λ^\pm are related to the probability of turning (see the derivation of model (1) in [31]), they are positive functions defined as:**

$$\begin{aligned} \lambda^\pm[u^+, u^-] &= \lambda_1 + \lambda_2 f(y_N[u^+, u^-]) + \lambda_3 f(y_D^\pm[u^+, u^-]) \\ &= \lambda_1 + \lambda_3 \left(\lambda_2^0 f(y_N[u^+, u^-]) + f(y_D^\pm[u^+, u^-]) \right), \end{aligned} \quad (2)$$

76 where we denote by $u = u^+ + u^-$ the total population density. In this paper, we
77 generalise the turning rates in [33, 32, 31] and assume that:

- 78 • individuals can turn randomly at a constant rate approximated by λ_1 [33];
- 79 • **individuals can turn randomly in response to the perception of individuals**
80 **inside any of the repulsive/attractive/alignment ranges (and independent of**
81 **the movement direction of their neighbours). These *non-directed interactions***
82 **with neighbours are described by the term $y_N[u^+, u^-]$ with turning rate λ_2 .**
- 83 • individuals can turn in response to interactions with neighbours positioned
84 within the repulsive (r), attractive (a) and alignment (al) zones, respectively
85 (see Figure 1(a)) [33]. This turning is *directed towards or away* from neigh-
86 bours, depending on the type of interaction (attractive or repulsive). For
87 alignment interactions, individuals turn to move in the same direction as their
88 neighbours. **The non-local *directed interactions* with neighbours are described**
89 **by terms $y_D^\pm[u^+, u^-]$ with turning rate λ_3 .**

90 If $\lambda_3 \neq 0$, we denote by λ_2^0 the quotient of the turning rates, λ_2/λ_3 . This choice
91 of notation is motivated by the corresponding 2D model (Section 3), the connection
92 between the 1D model (1) and the 2D model (18) will be made clearer in Remarks
93 3, 4, 5 and 6. The turning function $f(\cdot)$ is a non-negative, increasing, bounded
94 functional of the interactions with neighbours. An example of such function is
95 $f(Y) = 0.5 + 0.5 \tanh(Y - y_0)$ (see [32]), where y_0 is chosen such that when $Y = 0$
96 (i.e., no neighbours around), then $f(0) \approx 0$ and the turning is mainly random.

97 **To model the long-distance social interactions that lead to turning behaviours,**
98 **we define the interaction kernels in 1D, see Figure 1, as decreasing functions of the**
99 **distance between the reference position x (of the population density) and the mid**
100 **of the interaction ranges s_j , $j = r, al, a$,**

$$K_j(x) = \frac{1}{\sqrt{2\pi m_j^2}} e^{-(x-s_j)^2/(2m_j^2)}, \quad (3)$$

101 for $x > 0$ and zero otherwise, with $j = r, al, a$ denoting short-range repulsion (K_r),
102 medium-range alignment (K_{al}) and long-range attraction (K_a) interaction kernels.
103 Here, $m_j = s_j/8$ controls the width of the interaction range j .

For the non-directed density-dependent turning we define the turning kernel, $K^N(x) = \hat{K}^N(x) + \hat{K}^N(-x)$ with $\hat{K}^N = q_r K_r + q_{al} K_{al} + q_a K_a$ obtained by superimposing the kernels K_j , $j = r, al, a$. Here q_r , q_{al} and q_a represent the magnitudes of the repulsive, alignment and attractive social interactions. Note that in [32], $\lambda_2^0 = 0$ and the density-dependent non-directed turning term does not exist. However, in 2D, this term appears naturally when we incorporate random turning behaviour (as discussed in Section 3). With these notations we may define

$$y_N[u] = K^N * u, \quad \text{with } u = u^+ + u^-,$$

104 for the *non-directed* turning mechanisms. We assume here that individuals turn
105 randomly whenever they perceive other neighbours around (within the repulsive,
106 alignment and attractive ranges).

107 For the *directed* density-dependent turning, we define

$$y_D^\pm[u^+, u^-] = y_r^\pm[u^+, u^-] - y_a^\pm[u^+, u^-] + y_{al}^\pm[u^+, u^-]. \quad (4)$$

108 Here, $y_j^\pm[u^+, u^-]$, $j = r, al, a$, describe the directed turning in response to neighbours
109 within the repulsive (r), alignment (al) and attractive (a) social ranges (as in [33]).
110 As we will explain shortly, the direction of the turning will be given by incorporating
111 movement direction towards or away conspecifics. For this reason, y_a^\pm and y_r^\pm enter
112 equation (4) with opposite signs.

113 The density-dependent turnings depend greatly on how individuals communicate
114 with each other, namely whether they can emit (perceive) signals to (from) *all* or
115 *some* of their neighbours. Two particular situations, described by models called M2
116 and M4 as in [32] (see Figure 3) are considered:

- 117 • *Model M2*: Individuals communicate via omni-directional communication sig-
118 nals, and thus they can perceive *all* their neighbours positioned around them
119 within all social interaction ranges. For instance, the majority of mammals
120 communicate via a combination of visual, chemical and auditory signals, which
121 allows them to receive/send information from/to all their neighbours. With
122 this assumption (see Figure 3(a)), the terms $y_{r,a,al}^\pm$ are defined as follows:

$$y_{r,a}^\pm[u^+, u^-] = q_{r,a} \int_0^\infty K_{r,a}(s)(u(x \pm s) - u(x \mp s))ds, \quad (5a)$$

$$y_{al}^\pm[u^+, u^-] = q_{al} \int_0^\infty K_{al}(s)(u^\mp(x \mp s) + u^\mp(x \pm s) - u^\pm(x \mp s) - u^\pm(x \pm s))ds. \quad (5b)$$

123 Here, q_j describe the magnitudes of the social interactions associated to the
124 interaction kernels defined in (3). To understand the effect of these terms on
125 the turning rates, let us focus on y_r^+ , for example. If $u(x+s) > u(x-s)$, then
126 y_r^+ enters λ^+ with positive sign, suggesting a higher likelihood of turning,
127 to avoid collision with neighbours ahead at $x+s$. If, on the other hand,
128 $u(x+s) < u(x-s)$, then y_r^+ enters λ^+ with a negative sign, suggesting a
129 lower likelihood of turning. In this case, the individuals at x will keep moving
130 in the same direction, to avoid collision with neighbours behind at $x-s$. Note
131 that the directionality of neighbours influences only the alignment interactions
132 (the attractive and repulsive interactions being defined in terms of the total
133 density u). Also, for this particular model, the random density-dependent

134 terms are given by

$$y_N[u] = \int_0^\infty \hat{K}^N(s)(u(x+s) + u(x-s))ds. \quad (6)$$

135 • *Model M4*: Individuals communicate via unidirectional communication sig-
 136 nals, and thus they can perceive only those neighbours moving towards them.
 137 For example, birds communicate via directional sound signals, and to ensure
 138 an effective transmission of their signals they orient themselves towards their
 139 targeted receivers [12]. With this assumption (see Figure 3(b)), the terms
 140 $y_{r,a,al}^\pm$ are defined as follows:

$$y_{r,a,al}^\pm[u^+, u^-] = q_{r,a,al} \int_0^\infty K_{r,a,al}(s)(u^\mp(x \pm s) - u^\pm(x \mp s))ds. \quad (7)$$

141 Here, the directionality of neighbours influences all three social interactions.
 142 Moreover, for this model, the random density-dependent terms are given by

$$y_N[u^+, u^-] = \int_0^\infty \hat{K}^N(s)(u^-(x+s) + u^+(x-s))ds. \quad (8)$$

143 In this equation, we assume that individuals turn randomly in response to
 144 u^- and u^+ individuals (i.e., in (8) we add all perceived individuals; this
 145 is in contrast to equation (7), where we subtract individuals positioned ahead
 146 from individuals positioned behind, to impose directionality in the turning
 147 behaviour). Note that in (8), y_N does not depend anymore on $u = u^+ + u^-$
 148 (as in (6)), since the individuals at x cannot perceive all their neighbours at
 149 $x \pm s$.

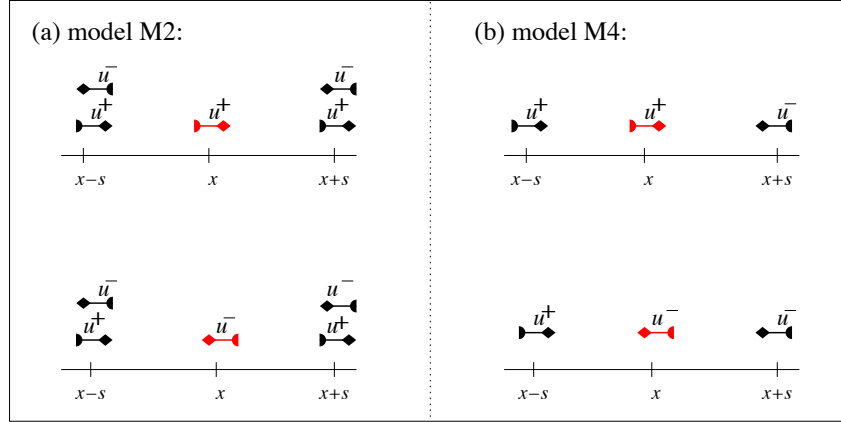


FIGURE 3. Diagram describing the mechanisms through which a reference individual positioned at x (right-moving – top; left-moving – bottom) perceives its neighbours positioned at $x-s$ and $x+s$. The reference individual can perceive (a) all its neighbours (model M2 in [32]); (b) only its neighbours moving towards it (model M4 in [32]).

150 We focus on these two particular models because: (i) the model (1)+(2)+(5)+(6)
 151 assuming $\lambda_1 = 0$ has been generalised to 2D; (ii) the model (1)+(2)+(7)+(8) as-
 152 suming $\lambda_2 = 0$ has been investigated analytically and numerically, and showed that

153 it can exhibit Hopf bifurcations (even when $q_{al} = 0$), which give rise to spatio-
 154 temporal patterns such as rotating waves and modulated rotating waves [14]. In
 155 contrast, model (1)+(2)+(5)+(6) with $\lambda_2 = 0$ does not seem to exhibit rotating
 156 waves when $q_{al} = 0$, see [32].

157 To complete the description of the model, we need to specify the domain size
 158 and the boundary conditions. Throughout most of this article, we will consider
 159 an infinite domain. However, for the purpose of numerical simulations, in Sections
 160 2.2 and 4 we will consider a finite domain of length L (i.e., $[0, L]$) with periodic
 161 boundary conditions: $u^+(L, t) = u^+(0, t)$, $u^-(0, t) = u^-(L, t)$. This assumption
 162 will also require wrap-around conditions for the kernels describing the nonlocal
 163 social interactions, see Section 4. For large L , this assumption approximates the
 164 dynamics on an infinite domain.

165 **In the following, we show how this hyperbolic 2-velocity model can be reduced**
 166 **to a parabolic equation by considering suitable scalings, which depend on the bio-**
 167 **logical phenomena and biological assumptions.** Of course, to be useful in practice,
 168 these parameters have to be calibrated and adapted to particular species as in
 169 [42, 43]. The scaling arguments are classically obtained by writing a dimensionless
 170 formulation of the problem. We refer to [57] in bacterial chemotaxis and [2] in semi-
 171 conductor modelling for a detailed description. After this dimensionless rescaling,
 172 we typically end up with two different time scales whose balance determines our
 173 small parameter: the drift time and the diffusion time.

174 We start in Subsection 2.1 with a parabolic scaling, which describes the situation
 175 where the drift time of a population is much smaller than its diffusion time. To this
 176 end, we discuss two separate cases (i.e., social interactions described by nonlinear
 177 or linear functions $f(y)$ in (2)), which lead to two different parabolic equations.

178 **2.1. Parabolic limit for non-linear interactions.** Next, we focus only on model
 179 M2 (i.e., equations (1)+(2)+(5)+(6)), since the results for model M4 are similar.
 180 The scaling argument applied in [44] transforms the hyperbolic system (1) into a
 181 parabolic equation. One can scale the space and time variables ($x = x^*/\varepsilon$, $t = t^*/\varepsilon^2$,
 182 with $\varepsilon \ll 1$), or can scale the speed (γ) and the turning rates ($\lambda_{1,2,3}$). In both cases,
 183 we consider the rescaled interaction kernels $K_j^*(x^*) = \frac{1}{\varepsilon} K_j(\frac{x^*}{\varepsilon})$ in the expressions
 184 for y_j^\pm , $j = r, al, a$. Here, we scale the time and space variables to be consistent with
 185 the approach in Section 3.1. As mentioned above, the scaling parameter ε depends
 186 on the biological problem modelled. For example, in [44] the authors connect ε
 187 to the ratio of the drift (τ_{drift}) and diffusion (τ_{diff}) times observed in bacteria
 188 such as *E. coli*, where $\tau_{drift} \approx 100$ seconds and $\tau_{diff} \approx 10^4$ seconds, and thus
 189 $\varepsilon \approx O(10^{-2})$. Similar scaling arguments are used in [57, Appendix] to analyse the
 190 ability of parabolic scalings to describe travelling pulses.

To perform the scaling, let us re-write model (1) in terms of the total density
 $u(x, t)$ and the flux $v(x, t) = \gamma(u^+(x, t) - u^-(x, t))$ of individuals (see also [44, 45]):

$$\varepsilon^2 \frac{\partial u}{\partial t} + \varepsilon \frac{\partial v}{\partial x} = 0, \quad (9a)$$

$$\varepsilon^2 \frac{\partial v}{\partial t} + \varepsilon \gamma^2 \frac{\partial u}{\partial x} = \gamma u (\lambda^- [u, v] - \lambda^+ [u, v]) - v (\lambda^+ [u, v] + \lambda^- [u, v]), \quad (9b)$$

191 with initial conditions $u(x, 0) = u_0(x)$, $v(x, 0) = v_0(x)$. For clarity, here we dropped
 192 the “*” from the rescaled space (x^*) and time (t^*) variables. In addition, we assume
 193 that individuals have a reduced perception of the surrounding neighbours for small

194 values of ε , [30]:

$$f_\varepsilon\left(y_D^\pm[u, v]\right) = \varepsilon f\left(y_D^\pm[u, \int_{x_\varepsilon^*} \varepsilon \frac{\partial u}{\partial t^*}\right], \quad f_\varepsilon\left(y_N[u]\right) = \varepsilon f\left(y_N[u]\right), \quad (10)$$

195 where f enters the turning functions λ^\pm (2):

$$\begin{aligned} \lambda^+[\cdot] + \lambda^-[\cdot] &= 2\lambda_1 + 2\lambda_2 \varepsilon f(y_N[\cdot]) + \varepsilon \lambda_3 \left(f(y_D^+[\cdot]) + f(y_D^-[\cdot])\right), \\ \lambda^-[\cdot] - \lambda^+[\cdot] &= \lambda_3 \varepsilon \left(f(y_D^-[\cdot]) - f(y_D^+[\cdot])\right). \end{aligned}$$

By eliminating $v = \varepsilon \int_x \frac{\partial u}{\partial t}$ from equations (9), and taking the limit $\varepsilon \rightarrow 0$, we obtain the following parabolic equation

$$\frac{\partial u}{\partial t} = \frac{\gamma^2}{2\lambda_1} \frac{\partial}{\partial x} \left(\frac{\partial u}{\partial x} \right) - \frac{\lambda_3 \gamma}{2\lambda_1} \frac{\partial}{\partial x} \left((f(y_D^-[u]) - f(y_D^+[u]))u \right). \quad (11)$$

196 We note here that the non-local terms $f(y_D^\pm[u])$ now depend only on the repulsive
197 and attractive interactions. The reason for this is that the alignment interactions
198 are defined in terms of $u^\pm = (u \pm \frac{1}{\gamma}v)/2 = 0.5(u \pm \frac{1}{\gamma} \int_{x/\varepsilon} \varepsilon^2 \partial u / \partial t)$. As $\varepsilon \rightarrow 0$, the
199 u terms in (5) cancel out, and the integrals approach zero. Equation (11) can be
200 re-written as

$$\frac{\partial u}{\partial t} = \frac{\partial}{\partial x} \left(D_0 \frac{\partial u}{\partial x} \right) - \frac{\partial}{\partial x} \left(B_0 u V(u) \right), \quad (12)$$

with diffusion rate $D_0 = \gamma^2/(2\lambda_1)$ and drift rate $B_0 = \lambda_3 \gamma/(2\lambda_1)$. The velocity $V(u)$ depends on the communication mechanism incorporated. For example, for model M2 we have $y_D^\pm[u] = \pm K * u$, and so the velocity is given by

$$V[u] = f(-K * u) - f(K * u)$$

where we define

$$\begin{aligned} K * u &= \bar{K}^+ * u - \bar{K}^- * u, \quad \bar{K}^\pm * u = \int_0^\infty \bar{K}(s) u(x \pm s) ds, \\ \bar{K} &= q_r K_r - q_a K_a. \end{aligned} \quad (13)$$

201 For model M4, we have $y_D^\pm[u] = \pm 0.5K * u$, and so the velocity is quite similar:
202 $V[u] = f(-0.5K * u) - f(0.5K * u)$, the factor 0.5 appearing from $u^\pm = 0.5(u \pm \frac{1}{\gamma}v)$.

203 **Remark 1.** We observe that the random density-dependent turning $f(y_N[u])$ does
204 not appear in this parabolic limit. This is the result of the scaling assumptions (10).

Remark 2. Here, the turning functions $f(\cdot)$ were chosen to be bounded, since individuals cannot turn infinitely fast when subject to very strong interactions with neighbours [32, 34]. However, for simplicity, many models consider linear functions: $f(z) = z$ (see, for example, [49, 51, 36]). The choice of having bounded or non-bounded turning functions $f(\cdot)$ has further implications on the models. In particular, for linear functions, the argument $y_D^\pm = y_r^\pm - y_a^\pm + y_{al}^\pm$ can be either positive or negative (depending on the magnitudes of the social interactions), with $y_D^+ = -y_D^-$. For very small constant and non-directional turning rates ($\lambda_1, \lambda_2 \approx 0$), this can lead to $\lambda^+ < 0$ and $\lambda^- > 0$, or vice versa. Now the $u^+ \lambda^+$ terms add to the $u^- \lambda^-$ terms, causing both u^+ and u^- populations to decide very fast to move in the same direction (in fact, one of the populations is reinforced to keep its moving direction). This is different from the case with bounded turning functions, where if $y_D^+ = -y_D^- \ll 0$, then $0 < \lambda^+ \approx \lambda_1 + \lambda_2 f(y_N[u^+, u^-]) < \lambda^-$. So if $\lambda_1, \lambda_2 \approx 0$,

then $u^+\lambda^+ \approx 0$ and hence population u^+ is not reinforced to keep its movement direction.

Because the 2D kinetic model that we will investigate in Section 3 assumes f to be a linear function, with a very weak directed turning behaviour ($\varepsilon\lambda_3$), we now consider the case $f(y_N[u]) = y_N[u] = K^N * u$ and $f(y_D^\pm[u]) = \varepsilon y_D^\pm[u]$, and so the turning rates can be written as

$$\lambda^\pm[u^+, u^-] = \lambda_1 + \lambda_2 K^N * u + \varepsilon \lambda_3 y_D^\pm[u] \quad (14)$$

By taking the limit $\varepsilon \rightarrow 0$ in (9), we obtain the following parabolic equation with density-dependent coefficients:

$$\frac{\partial u}{\partial t} = \frac{\partial}{\partial x} \left(D[u] \frac{\partial u}{\partial x} \right) - \frac{\partial}{\partial x} \left(B[u] u (y_D^-[u] - y_D^+[u]) \right), \quad (15a)$$

$$D[u] = \frac{\gamma^2}{2(\lambda_1 + \lambda_2 K^N * u)} \quad \text{and} \quad B[u] = \frac{\lambda_3 \gamma}{2(\lambda_1 + \lambda_2 K^N * u)}. \quad (15b)$$

205 This expression is similar to the asymptotic parabolic equation (30) for the 2D
206 model. We will return to this aspect in Section 3.1.

207 **2.2. The preservation of steady states and their stability as $\varepsilon \rightarrow 0$.** The
208 spatially homogeneous steady states describe the situation where individuals are
209 evenly spread over the whole domain. In the following we investigate how these
210 steady states and their linear stability are preserved in the parabolic limit. To this
211 end, we focus on the more general case of non-linear social interactions (the case
212 with linear interactions is similar). For simplicity we assume here that $\lambda_2 = 0$
213 and $q_{al} = 0$. To calculate these spatially homogeneous states we need to define
214 $A = \int_0^L (u^+ + u^-) dx$ the total population density. **For simplicity, throughout this**
215 **paper we assume that $A = 2$; similar results can be obtained for different values of**
216 **A .**

217 Figure 4(a) shows the number and magnitude of the steady states u^* displayed by
218 (9)-(10) with communication mechanism M4, for different values of ε , as one varies
219 the difference in the magnitude of the repulsive and attractive social interactions,
220 $q_r - q_a$. For **medium ε** , the model can display up to 5 different steady states: one
221 “unpolarised” state $(u^+, u^-) = (u^*, u^*) = (A/2, A/2)$ (where half of the individuals
222 are facing left and half are facing right), and two or four “polarised” states $(u^*, A -$
223 $u^*)$, $(A - u^*, u^*)$ characterised by $u^* < A/2$ or $u^* > A/2$. Two of these “polarised”
224 states exist only in a very narrow parameter range: e.g., for $\varepsilon = 1$, they exist when
225 $q_r - q_a \in (2, 3.7)$. The other two “polarised” states exist for any $q_r - q_a > 2$. **For a**
226 **calculation of the threshold values of $q_r - q_a$ that ensure the existence of 3 or 5 steady**
227 **states see [33].** As ε decreases, the magnitude of the polarised states decreases (i.e.,
228 the differences between the number of individuals facing right and those facing left
229 are decreasing). Moreover, for small ε , these polarised states appear only when
230 repulsion becomes much stronger than attraction (i.e., $q_r - q_a \gg 10$). When $\varepsilon = 0$
231 there is only one steady state $u^* = A/2$. Since this state exists for all $\varepsilon \geq 0$, from
232 now on we will focus our attention only on it. **Note that for $q_{al} = 0$ and for the**
233 **communication mechanism M2 (not shown here), the nonlocal attractive-repulsive**
234 **terms vanish, and there is only one steady state, $u^* = A/2 = 1$, which does not**
235 **depend on ε .**

236 Models (1) and (9) do exhibit a large variety of local bifurcations: codimension-
237 1 Steady-state and Hopf bifurcations [34] as well as codimension-2 Hopf/Hopf,

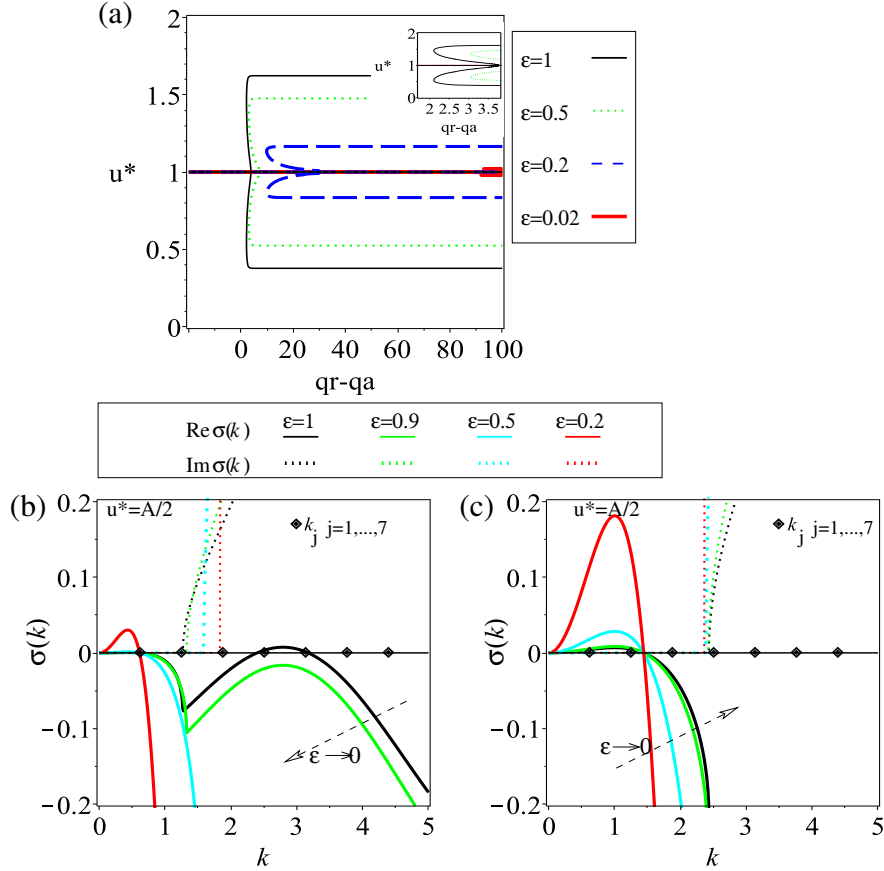


FIGURE 4. (a) Spatially homogeneous steady states u^* for model (9) with communication signals (7) and (8) (communication mechanism M4), for different values of ε . The small inset figure shows the 5 possible steady states occurring for $\varepsilon = 1$ and $q_r - q_a \in (2, 3.7)$ (see the black continuous curve); (b) Dispersion relation $\sigma(k_j)$ for M4 (given by (16)), showing the stability of the spatially homogeneous steady state $u^* = A/2$, for different values of ε ; (c) Dispersion relation $\sigma(k_j)$ for M2, for the stability of the spatially homogeneous steady state $u^* = A/2$, for different values of ε . The continuous curves describe $\text{Re } \sigma(k_j)$, while the dotted curves describe the $\text{Im } \sigma(k_j)$. The small diamond-shaped points show the discrete wavenumbers $k_j, j = 1, \dots, 7$, with $k_j = 2\pi j/L$ (and thus $k_j \in (0, 5)$ for $j = 1, \dots, 7$ and $L = 10$). The parameter values are: (b) $q_a = 1.545$, $q_r = 2.779$; (c) $q_a = 1.5$, $q_r = 0.93$. The rest of parameters are: $q_{a1} = 0$, $\lambda_1 = 0.2$, $\lambda_2 = 0$, $\lambda_3 = 0.9$, $A = 2$.

238 Hopf/Steady-state and Steady-state/Steady-state bifurcations [14]. Next we fo-
 239 cus on the parameter region where two such bifurcations can occur. We choose a
 240 Hopf/steady-state bifurcation for M4 (Figure 4(b)) and a steady-state bifurcation
 241 for M2 (Figure 4(c)), and investigate what happens when $\varepsilon \rightarrow 0$. To identify the

parameter regions where these bifurcations occur, we consider a finite domain of length L , and investigate the growth of small perturbations of spatially homogeneous solutions. We assume $u^\pm \propto u^* + a_\pm \exp(\sigma t + ik_j x)$, with $k_j = 2\pi j/L$, $j \in \mathbb{N}^+$, the discrete wave-numbers, and $|a_\pm| \ll 1$. We substitute these solutions into the linearised system (9), and by imposing that the determinant of this system is zero, we obtain the following dispersion relation, which connects σ (the growth/decay of the perturbations) with the wave-numbers k_j :

$$\varepsilon^2 \sigma^2 + \sigma(2L_1^\varepsilon - R_2^\varepsilon \operatorname{Re}(\hat{K}^+)) + \gamma^2 k_j^2 - \gamma k_j R_2 \operatorname{Im}(\hat{K}^+) = 0, \quad (16)$$

where $L_1^\varepsilon = \lambda_1 + \varepsilon \lambda_3 f(0)$, $R_2^\varepsilon = 2\varepsilon u^* \lambda_3 f'(0)$, and $\hat{K}^+ = \operatorname{Re}(\hat{K}^+) + i \operatorname{Im}(\hat{K}^+)$ the Fourier transforms of $\bar{K}^+ * u$ described in equations (13). Note that the wave numbers k_j that become unstable (i.e., for which $\operatorname{Re}(\sigma(k_j)) > 0$) determine, at least for a short time, the number of ‘‘peaks’’ j that emerge in the spatial distribution of the density.

Figure 4(b) shows the stability of the spatially homogeneous steady state $u^* = A/2$, for model M4, as given by the dispersion relation (16). Even if the wave-numbers k_j are discrete (see the diamond-shaped points on the x-axis of Figure 4(b)), we plot $\sigma(k_j)$, $j > 0$ as a continuous function of k_j for clarity. To discuss what happens with a Hopf bifurcation as $\varepsilon \rightarrow 0$, we focus in Figure 4(b) on a parameter space where such a bifurcation occurs (i.e., where $\operatorname{Re}(\sigma(k_j)) = 0$ in (16)): $q_a = 1.545$, $q_r = 2.779$, $\lambda_1 = 0.2$, $\lambda_2 = 0$, $\lambda_3 = 0.9$ and $\varepsilon = 1$ (see also [15]). For these parameter values, three modes become unstable at the same time: a steady-state mode k_1 ($\operatorname{Im}(\sigma(k_1)) = 0$; associated with stationary patterns with 1 peak) and two Hopf modes k_4 and k_5 ($\operatorname{Im}(\sigma(k_{4,5})) > 0$; associated with travelling patterns with 4 or 5 peaks). As $\varepsilon \rightarrow 0$, the steady-state mode persists while the Hopf modes disappear (i.e., $0 < \operatorname{Re}(\sigma(k_1)) \ll 1$ and $\operatorname{Re}(\sigma(k_{4,5})) < 0$; see Figure 4(b).) This can be observed also from equation (16): as $\varepsilon \rightarrow 0$, we have $\sigma \in \mathbb{R}$. A similar investigation of the local stability of the spatially homogeneous steady states associated with the non-local parabolic equation (12) shows that this equation cannot have complex eigenvalues (i.e., $\operatorname{Im}(\sigma(k_j)) = 0$ for all $j > 0$), and thus cannot exhibit local Hopf bifurcations [16].

Figure 4(c) shows the stability of the spatially homogeneous steady state $u^* = A/2$, for model M2, as given by the dispersion relation $\sigma(k_j)$:

$$\varepsilon^2 \sigma^2 + \sigma(2L_1^\varepsilon) + \gamma^2 k_j^2 - 2\gamma k_j R_2 \operatorname{Im}(\hat{K}^+) = 0. \quad (17)$$

For $q_a = 1.5$, $q_r = 0.93$, $\lambda_1 = 0.2$, $\lambda_2 = 0$, $\lambda_3 = 0.9$ and $\varepsilon = 1$, model M2 exhibits a steady-state bifurcation, i.e., $\operatorname{Re}(\sigma(k_j)) = \operatorname{Im}(\sigma(k_j)) = 0$ in (17). In particular, two steady-state modes are unstable at the same time: k_1 and k_2 (both associated with stationary patterns). As $\varepsilon \rightarrow 0$, the two modes remain unstable. Hence, we expect that the spatial patterns generated by these modes will persist as $\varepsilon \rightarrow 0$. We will return to this aspect in Section 4.4, when we will investigate numerically the mechanisms that lead to the disappearance of the Hopf modes and the persistence of the steady-state modes, as $\varepsilon \rightarrow 0$.

3. Description of 2D Models. An attempt to generalise a specific case of the 1D model (1)-(2)-(5)-(6) to two dimensions was made by Fetecau [36]. The Boltzmann-type model described in [36] incorporates the non-local social interactions in the

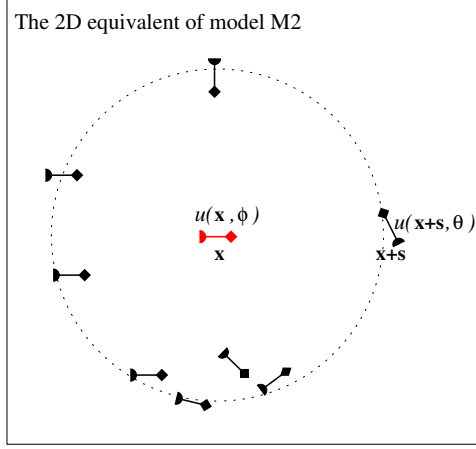


FIGURE 5. Caricature description of the M2 mechanism in 2D (where individuals can perceive *all* their neighbours within a certain interaction range). We assume that a reference individual is positioned at $\mathbf{x} = (x, y)$ and moves in direction ϕ . Its neighbours are at various spatial positions $\mathbf{x} + \mathbf{s}$ within a certain interaction range (e.g., alignment range). The interaction ranges are described by the 2D kernels (21); see also Figure 1(a).

284 reorientation terms:

$$\frac{\partial u}{\partial t} + \gamma \mathbf{e}_\phi \cdot \nabla_{\mathbf{x}} u = -\lambda(\mathbf{x}, \phi)u + \int_{-\pi}^{\pi} T(\mathbf{x}, \phi', \phi)u(\mathbf{x}, \phi', t)d\phi'. \quad (18)$$

285 Here, $u(\mathbf{x}, \phi, t)$ is the total population density of individuals located at $\mathbf{x} = (x, y)$,
 286 moving at a constant speed $\gamma > 0$ in direction ϕ . The term $\mathbf{e}_\phi = (\cos(\phi), \sin(\phi))$
 287 gives the movement direction of individuals. The reorientation terms, $\lambda(\mathbf{x}, \phi)$ and
 288 $T(\mathbf{x}, \phi', \phi)$ depend on the non-local interactions with neighbours, which can be
 289 positioned in the repulsive, attractive, and alignment ranges depicted in Fig. 1(a).
 290 Thus, these terms have three components each, corresponding to the three social
 291 interactions:

$$T(\mathbf{x}, \phi', \phi) = T_{al}(\mathbf{x}, \phi', \phi) + T_a(\mathbf{x}, \phi', \phi) + T_r(\mathbf{x}, \phi', \phi).$$

In contrast to the model in [36], here we assume that the reorientation terms

$$\lambda_j(\mathbf{x}, \phi') = \int_{-\pi}^{\pi} T_j(\mathbf{x}, \phi', \phi)d\phi, \quad j = r, a, al$$

have both a constant and a density-dependent component:

$$T_{al}(\mathbf{x}, \phi', \phi) = \frac{\eta_{al}}{2\pi} + \quad (19a)$$

$$\lambda_3 q_{al} \int_{-\pi}^{\pi} \int_{\mathbb{R}^2} K_{al}^d(\mathbf{x} - \mathbf{s})K_{al}^o(\theta, \phi')\omega_{al}(\phi' - \phi, \phi' - \theta)u(\mathbf{s}, \theta, t)dsd\theta,$$

$$T_{r,a}(\mathbf{x}, \phi', \phi) = \frac{\eta_{r,a}}{2\pi} + \quad (19b)$$

$$\lambda_3 q_{r,a} \int_{-\pi}^{\pi} \int_{\mathbb{R}^2} K_{r,a}^d(\mathbf{x} - \mathbf{s})K_{r,a}^o(\mathbf{s}, \mathbf{x}, \phi')\omega_{r,a}(\phi' - \phi, \phi' - \psi)u(\mathbf{s}, \theta, t)dsd\theta.$$

292 Therefore, the turning rate $\lambda(\mathbf{x}, \phi) = \lambda_{al}(\mathbf{x}, \phi) + \lambda_a(\mathbf{x}, \phi) + \lambda_r(\mathbf{x}, \phi)$ is defined by

$$\lambda = \lambda_1 + \lambda_3 \bar{\lambda}[u(\mathbf{x}, \phi)], \quad (20)$$

293 with $\lambda_1 = \eta_r + \eta_{al} + \eta_a$ and $\bar{\lambda}[u(\mathbf{x}, \phi)]$ being given as the integral over $\phi' \in [-\pi, \pi]$
 294 of the sum of nonlocal terms in (19) with ϕ and ϕ' interchanged.

295 **Remark 3.** By defining the constant basic turning rate to be $\lambda_1 = \eta_r + \eta_{al} + \eta_a$, we
 296 generalised the model in [36] (where $\lambda_1 = 0$). Note that the turning rates here are
 297 linear functions of the non-local interactions with neighbours. This is in contrast to
 298 the more general non-linear turning function f we considered in Section 2.1 for the
 299 1D hyperbolic model. In what follows, we are interested in non-constant turning
 300 rates $\lambda_j(\mathbf{x}, \phi')$, $j = r, a, al$, and so we will henceforth assume $\lambda_3 \neq 0$.

301 As in [36], λ_j , $j = r, a, al$, are defined in terms of both distance kernels and
 302 orientation kernels. The 2D distance kernels K_j^d , $j = r, a, al$ are given by

$$K_j^d(\mathbf{x}) = \frac{1}{A_j} e^{-(\sqrt{x^2+y^2}-d_j)/m_j^2}, \quad j = r, a, al, \quad (21)$$

303 where constants A_j are chosen such that the kernels integrate to one. The orient-
 304 ation kernels K_j^o measure the likelihood of turning in response to the movement
 305 direction of neighbours (for alignment interactions) or in response to the position
 306 of neighbours (for repulsive and attractive interactions):

$$\begin{aligned} K_{al}^o(\theta, \phi) &= \frac{1}{2\pi} (1 - \cos(\phi - \theta)), \\ K_{r,a}^o(\mathbf{s}, \mathbf{x}, \phi) &= \frac{1}{2\pi} (1 \pm \cos(\phi - \psi)), \end{aligned}$$

where ψ is the angle between the positive x -axis and the relative location $\mathbf{s} - \mathbf{x}$ of the
 neighbours at \mathbf{s} with respect to the reference individual at \mathbf{x} . Finally, ω describes
 the tendency to turn from direction ϕ' to direction ϕ , as a result of interactions
 with individuals moving in direction θ :

$$\omega(\phi' - \phi, \phi' - \theta) = g(\phi' - \phi - R(\phi' - \theta)),$$

for some suitable choice of g . Note that in the case $\lambda_1 = 0$, the function ω describes
 the probability of re-orientation in the sense discussed in [38] and thus we require
 $\int \omega(\phi' - \phi, \phi' - \theta) d\phi = 1$. For example, g could be a periodic function that integrates
 to one:

$$g(\theta) = \frac{1}{\sqrt{\pi}\sigma} \sum_{z \in \mathbb{Z}} e^{-(\frac{\theta+2\pi z}{\sigma})^2}, \quad \theta \in (-\pi, \pi),$$

307 with σ a parameter measuring the uncertainty of turning (with small σ leading to
 308 exact turning) [36, 37]. Another typical choice could be the von Mises distribution,
 309 as in Vicsek-type models [27].

310 On the other hand, when $\lambda_1 > 0$, then g can be interpreted as a small reorientation
 311 perturbation from the random turning behaviour and so ω satisfies $\int \omega(\phi' - \phi, \phi' -$
 312 $\theta) d\phi = 0$ and therefore g is required to be odd.

Remark 4. Fetecau [36] showed that by imposing the turning angle to have only
 two possible values $\phi = \pm\pi$, the 2D model (18) can be reduced to the 1D model
 (1) for a specific choice of turning rates $\lambda^\pm[u^+, u^-]$. More precisely, considering
 the more general turning operators (19a) and (19b), we recover (2) with $\lambda_1, \lambda_3 \geq$

0, $\lambda_2 = 0$ for a linear turning function $f(z) = z$, and with the communication mechanism

$$\begin{aligned} y_D^\pm[u^+, u^-] &= \frac{1}{\pi} q_{al} \int_{-\infty}^{\infty} K_{al}(x-s) (u^\mp(s, t)) ds \\ &\quad + \frac{1}{\pi} q_a \int_{-\infty}^x K_a(x-s) (u^+(s, t) + u^-(s, t)) ds \\ &\quad + \frac{1}{\pi} q_r \int_x^{\infty} K_r(x-s) (u^+(s, t) + u^-(s, t)) ds. \end{aligned}$$

313 This is a similar turning behaviour to model M2 in [32], since individuals receive
314 and emit omni-directional communication signals, but with the function f linear.
315 Moreover, as we will show in the next section, even if the 2D model (18) can be
316 reduced to a special case of the 1D model (1) without λ_2 in (2), the parabolic scaling
317 of the 2D model reduces to a special case of the parabolic scaling of the 1D model,
318 which includes a λ_2 term for non-directed turning. As we will see shortly, this
319 2D parabolic scaling leads to the natural appearance of a non-directed interaction
320 contribution, suggesting that there are more subtle differences between the 1D and
321 2D models.

322 The diffusion limit (i.e., $x = x^*/\varepsilon$, $t = t^*/\varepsilon^2$) of a transport model similar to
323 (18), but with constant turning rates λ was discussed in [44, 54]. In the following we
324 consider the parabolic limit for model (18) with density-dependent turning rates.

325 **3.1. Parabolic Drift-Diffusion limit.** We focus on the case where individuals are
326 only influenced slightly by the presence of neighbours, i.e., the turning mechanism
327 can be assumed to be a small perturbation of a uniform turning probability. In
328 this case, we will show that the Boltzmann-type equation (18) can be reduced to a
329 drift-diffusion equation in the macroscopic regime.

330 We consider the scaling $t = t^*/\varepsilon^2$, $\mathbf{x} = \mathbf{x}^*/\varepsilon$, where $\varepsilon \ll 1$ is a small parameter.
331 Since the velocity in the new variables is of order $1/\varepsilon$, then we make the scaling
332 assumption that an individual's turning behaviour is only influenced slightly by the
333 presence of neighbours:

$$T[u](\mathbf{x}, \phi', \phi) = \frac{\lambda_1}{2\pi} + \frac{\lambda_2}{2\pi} K^d * \rho(\mathbf{x}, t) + \varepsilon \lambda_3 B[u](\mathbf{x}, \phi', \phi), \quad (22)$$

with $\rho(\mathbf{x}, t) = \int_{-\pi}^{\pi} u(\mathbf{x}, \phi, t) d\phi$, and where we define

$$K^d(\mathbf{x}) := q_{al} K_{al}^d(\mathbf{x}) + q_a K_a^d(\mathbf{x}) + q_r K_r^d(\mathbf{x})$$

334 to be the *social distance kernel*. As we have done in the 1D case, we have separated
335 the non-directed and directed turning rates.

336 If $\lambda_3 \neq 0$, we factorise again the turning rate λ_3 corresponding to the directed
337 interactions and write $\lambda_2^0 = \lambda_2/\lambda_3$ the quotient of turning rates. With this notation,
338 $\bar{\lambda}[u(\mathbf{x}, \phi)]$ in (20) can be written as

$$\bar{\lambda}[u(\mathbf{x}, \phi)] = \lambda_2^0 K^d * u(\mathbf{x}, \phi, t) + \varepsilon y_D[u(\mathbf{x}, \phi, t)], \quad (23)$$

with $y_D[u] = \int B[u](\mathbf{x}, \phi', \phi) d\phi'$. Note that the turning rate λ given by (20)-(23)
corresponds to the 1D turning rates (14) with this specific choice of $y_D[u]$. The
scaling assumption (22) can be derived by introducing reduced perception of direc-
tionality of neighbours into the re-orientation function ω and into the orientation

kernels K_j^o ,

$$\begin{aligned} g_j(\vartheta) &= \lambda_2^0 + \varepsilon G_j(\vartheta), \\ K_{al}^o(\theta, \phi) &= \frac{1}{2\pi} (1 - \varepsilon \cos(\phi - \theta)), \\ K_{r,a}^o(\mathbf{s}, \mathbf{x}, \phi) &= \frac{1}{2\pi} (1 \pm \varepsilon \cos(\phi - \psi)), \end{aligned}$$

339 where $G_j(\vartheta)$, $j = r, a, al$ are *signal response functions* to be chosen according to
 340 the biological context. Substituting these expressions into the reorientation terms
 341 (19), we define $\lambda_1 = \eta_{al} + \eta_r + \eta_a$ and we obtain (22) with a precise expression for
 342 the *social response function* $B[u]$.

If $\lambda_1 = 0$, we further have $\lambda_2 = \lambda_3/2\pi$ and $\int_{-\pi}^{\pi} G_j(\phi' - \phi - R(\phi' - \theta))d\phi = 0$,
 $j = r, a, al$ as the probability to turn to any new angle is 1. In addition, we want
 the turning function $R(\vartheta)$ to be close to an unbiased turning mechanism. This can
 be expressed by taking $R(\vartheta) = \varepsilon\vartheta$, which indeed corresponds to weak interaction
 between individuals, [38]. We obtain $B[u] = B_{al}[u] + B_a[u] + B_r[u]$ with

$$\begin{aligned} B_{al}[u](\phi', \phi) &= \frac{1}{2\pi} q_{al} G_{al}(\phi' - \phi) K_{al}^d * \rho(\mathbf{x}, t) \\ &\quad - \frac{\lambda_2^0}{2\pi} q_{al} \int_{\mathbb{R}^2} K_{al}^d(\mathbf{x} - \mathbf{s}) \int_{-\pi}^{\pi} \cos(\phi' - \theta) u(\mathbf{s}, \theta, t) d\theta ds, \end{aligned} \quad (24)$$

$$\begin{aligned} B_{r,a}[u](\phi', \phi) &= \frac{1}{2\pi} q_{r,a} G_{r,a}(\phi' - \phi) K_{r,a}^d * \rho(\mathbf{x}, t) \\ &\quad \pm \frac{\lambda_2^0}{2\pi} q_{r,a} \int_{\mathbb{R}^2} K_{r,a}^d(\mathbf{x} - \mathbf{s}) \cos(\phi' - \psi) \rho(\mathbf{s}, t) ds. \end{aligned} \quad (25)$$

343

344 **Remark 5.** Note that in 2D, λ_2^0 is introduced as the relative strength of non-
 345 directed and directed turning kernels. This is part of the scaling assumption in 2D,
 346 whereas in 1D, we introduced it as part of the model (1)-(2) before rescaling. Note
 347 that $\lambda_2^0 = 1/2\pi$ in Fetecau's model where no distinction is made between directed
 348 and non-directed turning.

Let us introduce

$$K_*^d(\mathbf{x}^*) = \frac{1}{\varepsilon} K^d\left(\frac{\mathbf{x}^*}{\varepsilon}\right), \quad B_*(\mathbf{x}^*, \phi', \phi) = \frac{1}{2\pi} B\left(\frac{\mathbf{x}^*}{\varepsilon}, \phi', \phi\right).$$

Simplifying the notation by dropping $*$, system (18) writes in the new variables as

$$\begin{aligned} \varepsilon^2 \partial_t u + \varepsilon \gamma \mathbf{e}_\phi \cdot \nabla_{\mathbf{x}} u &= \frac{1}{2\pi} (\lambda_1 + \lambda_2 K^d * \rho) (\rho - 2\pi u) \\ &\quad + \varepsilon \lambda_3 2\pi \int_{-\pi}^{\pi} B(\mathbf{x}, \phi', \phi) u(\mathbf{x}, \phi', t) d\phi' \\ &\quad - \varepsilon \lambda_3 2\pi u(\mathbf{x}, \phi, t) \int_{-\pi}^{\pi} B(\mathbf{x}, \phi, \phi') d\phi'. \end{aligned} \quad (26)$$

Using a Hilbert expansion approach, $u = u_0 + \varepsilon u_1 + \varepsilon^2 u_2 + \dots$, and defining the macroscopic densities $\rho_i = \int_{-\pi}^{\pi} u_i d\phi$ for $i \in \mathbb{N}_0$, we obtain at leading order a relaxation towards a uniform angular distribution at each position:

$$\begin{aligned} u_0(\mathbf{x}, \phi, t) &= \rho_0(\mathbf{x}, t) F(\phi), \\ F(\phi) &= \frac{1}{2\pi} \mathbb{1}_{\phi \in (-\pi, \pi]}. \end{aligned} \quad (27)$$

349 Integrating (26) with respect to the direction of motion ϕ , we obtain the continuity
350 equation

$$\partial_t \rho_0 + \gamma \int_{-\pi}^{\pi} \mathbf{e}_\phi \cdot \nabla_{\mathbf{x}} u_1 d\phi = 0. \quad (28)$$

Comparing orders of ε and using (27), we can derive an expression for u_1 in terms of u_0, ρ_0, ρ_1 ,

$$\begin{aligned} u_1 = & \frac{1}{2\pi} \rho_1 - \gamma \frac{\mathbf{e}_\phi \cdot \nabla_{\mathbf{x}} u_0}{\lambda_1 + \lambda_2 K^d * \rho_0} \\ & + \rho_0 \frac{\lambda_3}{\lambda_1 + \lambda_2 K^d * \rho_0} \int_{-\pi}^{\pi} B[\rho_0](\mathbf{x}, \phi', \phi) - B[\rho_0](\mathbf{x}, \phi, \phi') d\phi'. \end{aligned}$$

Substituting into (28), we arrive at a macroscopic drift-diffusion equation of the form

$$\partial_t \rho_0 = \nabla_{\mathbf{x}} \cdot (D[\rho_0] \nabla_{\mathbf{x}} \rho_0 - \rho_0 \mathbf{k}[\rho_0]),$$

351 where the macroscopic diffusion coefficient $D[\rho_0] = \gamma^2 / (2(\lambda_1 + \lambda_2 K^d * \rho_0))$ and the
352 social flux

$$\mathbf{k}[\rho_0] = \frac{\lambda_3 \gamma}{\lambda_1 + \lambda_2 K^d * \rho_0} \int_{-\pi}^{\pi} \int_{-\pi}^{\pi} (\mathbf{e}_\phi - \mathbf{e}_{\phi'}) B[\rho_0](\mathbf{x}, \phi', \phi) d\phi' d\phi \quad (29)$$

353 are both described in terms of microscopic quantities. In the context of collective
354 behaviour of animal groups, we make two further assumptions:

- (i) Individuals can process information in a similar manner for all three types of social interactions:

$$G_{al}(\vartheta) = G_r(\vartheta) = G_a(\vartheta) =: G(\vartheta) \quad \forall \vartheta.$$

- 355 (ii) Individuals have symmetric perception, in other words, they can process in-
356 formation equally well from left and right. Then the turning probability function
357 ω is bisymmetric,

$$\omega(-\alpha, -\beta) = \omega(\alpha, \beta),$$

358 which implies symmetry of the signal response function G .

Under these assumptions, the first term of the social response functions $B_j[u]$ in (24) and (25) cancels when substituted into the social flux (29). The second term contains the factor λ_2^0 which cancels with λ_3 in (29), leaving us with a factor of λ_2 in the social flux. Using (27), we can simplify the social flux even further and obtain the drift-diffusion equation

$$\partial_t \rho = \nabla_{\mathbf{x}} \cdot (D_0[\rho] \nabla_{\mathbf{x}} \rho) - \nabla_{\mathbf{x}} \cdot (\rho \mathbf{k}[\rho]), \quad (30a)$$

$$D_0[\rho] = \frac{\gamma^2}{2(\lambda_1 + \lambda_2 K^d * \rho)}, \quad (30b)$$

$$\mathbf{k}[\rho](\mathbf{x}, t) = \frac{\lambda_2 \pi \gamma}{\lambda_1 + \lambda_2 K^d * \rho} \left(q_r K_r^d(\mathbf{x}) \frac{\mathbf{x}}{|\mathbf{x}|} - q_a K_a^d(\mathbf{x}) \frac{\mathbf{x}}{|\mathbf{x}|} \right) * \rho. \quad (30c)$$

359 For notational convenience, we dropped the zero in ρ_0 . Note that this equation is
360 similar to the 1D drift-diffusion equation (15) obtained via the parabolic limit for
361 linear social interactions.

Remark 6. Integrating the 2D scaling assumption (22), we have

$$\lambda(\mathbf{x}, \phi') = \lambda_1 + \lambda_2 K^d * \rho(\mathbf{x}, t) + \varepsilon \lambda_3 \int B[u](\mathbf{x}, \phi', \phi) d\phi,$$

which is a particular case of the 1D scaling assumption (14). More precisely, the 2D turning rate $\lambda(\mathbf{x}, \phi')$ corresponds to (2) on the projected velocity set $\{0, \pi\}$, with a linear turning function $f(z) = z$ and with the non-directed and directed communication mechanisms given by

$$\begin{aligned} y_N[u] &= K^d * \rho(\mathbf{x}, t), \\ y_D^\pm[u^+, u^-] &= \frac{G(0) + G(\pi)}{2} K^d * \rho(\mathbf{x}, t) \\ &\mp \lambda_2^0 \int_{\mathbb{R}} q_{al} K_{al}^d(\mathbf{x} - \mathbf{s}) (u^+(s_1, t) - u^-(s_1, t)) ds_1 \\ &\mp \lambda_2^0 \int_{-\infty}^{x_1} (q_r K_r^d(\mathbf{x} - \mathbf{s}) - q_a K_a^d(\mathbf{x} - \mathbf{s})) \rho(\mathbf{s}, t) ds_1 \\ &\pm \lambda_2^0 \int_{x_1}^{\infty} (q_r K_r^d(\mathbf{x} - \mathbf{s}) - q_a K_a^d(\mathbf{x} - \mathbf{s})) \rho(\mathbf{s}, t) ds_1, \end{aligned} \quad (31)$$

362 where $\mathbf{x} = (x_1, 0)$, $\rho(\mathbf{x}, t) = u^+(x_1, t) + u^-(x_1, t) = u(x_1, t)$, and where we used as-
 363 sumptions (i) and (ii). Hence, model (1)-(14) with communication mechanism (31)
 364 corresponds exactly to the 2D non-local kinetic model (18)-(22)-(24)-(25). This
 365 means, for instance, that the macroscopic 2D model (30) reduces to the heat equa-
 366 tion for $\lambda_2 = 0$, which is not the case in the parabolic limit (15) of the corresponding
 367 1D hyperbolic model (1) with the turning rates given by (2). In fact, our 2D scaling
 368 assumption $g_j(\vartheta) = \lambda_2^0 + \varepsilon G_j(\vartheta)$, $j = al, r, a$, introduces the relative strength of
 369 directed and non-directed turning kernels into the expression of the social response
 370 function $B[u]$, which is responsible for the appearance of a factor λ_2 in the drift of
 371 the macroscopic 2D model (30).

372 **Remark 7.** For some particular choices of distance kernels, the limiting parabolic
 373 model (30) can be reduced to well known equations. Let us assume, for example,
 374 that the distance kernels are constant on the whole domain,

$$K_j^d(\mathbf{x}) = 1, \quad j = al, a, r. \quad (32)$$

375 This assumption corresponds to a setting in which individuals interact equally well
 376 with all other individuals present in the entire domain. This is true locally for
 377 example if we have many individuals packed in little space. Under assumption (32)
 378 together with $\lambda_1 = 0$, model (30) simplifies to

$$\partial_t \rho = \frac{C_0}{\lambda_2} \Delta \rho + C_1 \nabla \cdot \left(\rho \int_{\mathbb{R}^2} \mathbf{e}_\psi \rho(\mathbf{s}) ds \right),$$

where

$$\mathbf{e}_\psi = \frac{\mathbf{s} - \mathbf{x}}{|\mathbf{s} - \mathbf{x}|},$$

379 and C_0, C_1 are constants depending only on γ, q_{al}, q_a, q_r and the total mass $\int \rho d\mathbf{x}$.
 380 If $q_a = q_r$, then the attraction and repulsion forces cancel out ($C_1 = 0$) and we
 381 obtain the heat equation. Let us henceforth assume $q_a \neq q_r$. Furthermore, we can
 382 write the social flux as

$$\mathbf{k}[\rho] = \nabla W * \rho, \quad (33)$$

where the interaction potential $W : \mathbb{R}^2 \rightarrow \mathbb{R}$ is given by $W(\mathbf{x}) = C_1 |\mathbf{x}|$. In fact, for
 the more general distance kernels (21) the social flux can also be written in the form
 (33), with the interaction potential W behaving like $|\mathbf{x}|$ close to zero and decaying

exponentially fast as $|\mathbf{x}| \rightarrow \infty$ (e.g. Morse potentials). Therefore, we recover the diffusive aggregation equation

$$\partial_t \rho = \Delta \rho + \nabla \cdot (\rho (\nabla W * \rho)),$$

383 which models the behaviour of particles interacting through a pairwise potential
 384 while diffusing with Brownian motion. This type of equation has received a lot of
 385 attention in recent years because of its ubiquity in modelling aggregation processes,
 386 such as collective behaviour of animals [50, 52, 9, 26] and bacterial chemotaxis [10]
 387 (see also the references therein).

388 **3.2. Grazing collision limit.** In the following, we consider another type of scaling
 389 that leads to parabolic equations, by focusing on the case where individuals turn
 390 only a small angle upon interactions with neighbours. This is biologically realistic
 391 as, for example, many migratory birds follow favourable winds or magnetic fields
 392 [53] and social interactions with neighbours might not have a considerable impact
 393 on directional changes of individuals. The so-called *grazing collisions*, i.e. collisions
 394 with small deviation, correspond to this assumption. In this case, we show that the
 395 Boltzmann-type equation (18) can be reduced to a Fokker-Planck equation with
 396 non-local advective and diffusive terms in the orientation space.

For simplicity, the 2D kinetic model (18) can be re-written as

$$\frac{\partial u}{\partial t} + \gamma e_\phi \nabla_x u = -Q^-[u] + Q^+[u, u],$$

with

$$\begin{aligned} Q^-[u] &= Q_r^-[u] + Q_a^-[u] + Q_{al}^-[u], & Q^+[u, u] &= Q_r^+[u, u] + Q_a^+[u, u] + Q_{al}^+[u, u], \\ Q_j^-[u] &= \lambda_j(x, \phi)u, & Q_j^+[u, u] &= \int_{-\pi}^{\pi} T_j(x, \phi', \phi)u(x, \phi', t)d\phi', \quad \text{for } j = r, al, a. \end{aligned}$$

Let us focus for now only on the alignment interactions; the analysis of attraction and repulsion interactions is similar. The grazing collision assumption suggests that we can rescale the probability of re-orientation as follows:

$$\omega_{al}^\varepsilon(\phi - \phi', \phi - \theta) = \frac{1}{\varepsilon} g_\varepsilon \left(\frac{\phi - \phi' - \varepsilon R(\phi - \theta)}{\varepsilon} \right).$$

397 Here, the parameter ε is related to the small re-orientation angle following interac-
 398 tions with neighbours moving in direction θ . If we denote by $\varepsilon\beta = \phi - \phi' - \varepsilon R(\phi - \theta)$,
 399 then since ω_ε integrates to 1, we obtain:

$$1 = \int_{-\pi}^{\pi} \omega_{al}^\varepsilon(\phi - \phi', \phi - \theta) d\phi' = \int_{-\pi + \phi - R(\phi - \theta)}^{\pi + \phi - R(\phi - \theta)} g_\varepsilon(\beta) d\beta = \int_{-\pi}^{\pi} g_\varepsilon(\beta) d\beta,$$

400 by periodicity of g_ε .

Generally, when an interaction kernel in the Boltzmann equation presents a singularity point, the troubles are avoided by considering a weak formulation of the Boltzmann operator [40, 20]. Expanding $Q_{al}[u] := -Q_{al}^-[u] + Q_{al}^+[u, u]$, we obtain

for all $\psi \in C_c^\infty([-\pi, \pi])$,

$$\begin{aligned} \int_{-\pi}^{\pi} Q_{al}[u]\psi(\phi)d\phi &= \eta_{al} \int_{-\pi}^{\pi} \left(\frac{1}{2\pi} \rho(x, t) - u(x, \phi, t) \right) \psi(\phi) d\phi \\ &+ \int_{-\pi}^{\pi} \int_{-\pi}^{\pi} \int_{\mathbb{R}^2} \lambda_3 q_{al} K_{al}^d(x-s) K_{al}^0(\theta, \phi) u(x, \phi, t) u(s, \theta, t) \cdot \\ &\int_{-\pi}^{\pi} \omega_{al}^\varepsilon(\phi - \phi', \phi - \theta) [\psi(\phi') - \psi(\phi)] d\phi' ds d\theta d\phi. \end{aligned} \quad (35)$$

By substituting $\phi' = \phi - \varepsilon\beta - \varepsilon R(\phi - \theta)$ into the $\psi(\phi')$ term in (35), and then expanding in Taylor series about ϕ we obtain:

$$\begin{aligned} \int_{-\pi}^{\pi} \omega_{al}^\varepsilon(\phi - \phi', \phi - \theta) [\psi(\phi') - \psi(\phi)] d\phi' &\approx \\ \int_{-\pi}^{\pi} g_\varepsilon(\beta) \left[(-\varepsilon\beta - \varepsilon R(\phi - \theta)) \frac{\partial \psi}{\partial \phi} + \frac{\varepsilon^2}{2} (\beta + R(\phi - \theta))^2 \frac{\partial^2 \psi}{\partial \phi^2} \right] d\beta. \end{aligned}$$

401 Equation (35) can thus be approximated by

$$\begin{aligned} \int_{-\pi}^{\pi} Q_{al}[u]\psi(\phi)d\phi &= \eta_{al} \int_{-\pi}^{\pi} \left(\frac{1}{2\pi} \rho(x, t) - u(x, \phi, t) \right) \psi(\phi) d\phi \\ &- \int_{-\pi}^{\pi} \frac{\partial}{\partial \phi} \left[u(x, \phi, t) C_{al}^\varepsilon[u, x, \phi] \right] \psi(\phi) d\phi \\ &+ \int_{-\pi}^{\pi} \frac{\partial^2}{\partial \phi^2} \left[u(x, \phi, t) D_{al}^\varepsilon[u, x, \phi] \right] \psi(\phi) d\phi, \end{aligned}$$

402 with the definitions

$$\begin{aligned} C_{al}^\varepsilon[u, x, \phi] &= \int_{-\pi}^{\pi} \int_{\mathbb{R}^2} \lambda_3 q_{al} K_{al}^d(x-s) K_{al}^0(\theta, \phi) A_{al}^\varepsilon(\phi - \theta) u(s, \theta, t) d\theta ds, \\ D_{al}^\varepsilon[u, x, \phi] &= \int_{-\pi}^{\pi} \int_{\mathbb{R}^2} \lambda_3 q_{al} K_{al}^d(x-s) K_{al}^0(\theta, \phi) B_{al}^\varepsilon(\phi - \theta) u(s, \theta, t) d\theta ds, \end{aligned}$$

403 where

$$\begin{aligned} A_{al}^\varepsilon(\phi - \theta) &= -\varepsilon (M_1(\varepsilon) + M_0(\varepsilon) R(\phi - \theta)), \\ B_{al}^\varepsilon(\phi - \theta) &= \frac{\varepsilon^2}{2} (M_2(\varepsilon) + 2M_1(\varepsilon) R(\phi - \theta) + M_0(\varepsilon) R(\phi - \theta)^2), \end{aligned}$$

404 and $M_n(\varepsilon) = \int_{-\pi}^{\pi} \beta^n g_\varepsilon(\beta) d\beta$, $n = 0, 1, 2$, denote the moment generating functions
405 of $g_\varepsilon(\beta)$. In a similar manner we can approximate the attractive and repulsive
406 non-local terms:

$$\begin{aligned} \int_{-\pi}^{\pi} Q_{r,a}[u]\psi(\phi)d\phi &= \eta_{r,a} \int_{-\pi}^{\pi} \left(\frac{1}{2\pi} \rho(x, t) - u(x, \phi, t) \right) \psi(\phi) d\phi \\ &- \int_{-\pi}^{\pi} \frac{\partial}{\partial \phi} \left(u(x, \phi, t) C_{r,a}^\varepsilon[u, x, \phi] \right) \psi(\phi) d\phi \\ &+ \int_{-\pi}^{\pi} \frac{\partial^2}{\partial \phi^2} \left(u(x, \phi, t) D_{r,a}^\varepsilon[u, x, \phi] \right) \psi(\phi) d\phi, \end{aligned}$$

where

$$\begin{aligned}
C_{r,a}^\varepsilon[u, x, \phi] &= \int_{-\pi}^{\pi} \int_{\mathbb{R}^2} \lambda_3 q_{r,a} K_{r,a}^d(x-s) K_{r,a}^0(s, x, \phi) A_{r,a}^\varepsilon(s, x, \phi) u(s, \theta, t) ds d\theta, \\
D_{r,a}^\varepsilon[u, x, \phi] &= \int_{-\pi}^{\pi} \int_{\mathbb{R}^2} \lambda_3 q_{r,a} K_{r,a}^d(x-s) K_{r,a}^0(s, x, \phi) B_{r,a}^\varepsilon(s, x, \phi) u(s, \theta, t) ds d\theta, \\
A_{r,a}^\varepsilon(s, x, \phi) &= -\varepsilon(M_1(\varepsilon)M_0(\varepsilon)R(\phi - \psi_s)), \\
B_{r,a}^\varepsilon(s, x, \phi) &= \frac{\varepsilon^2}{2} \left[M_2(\varepsilon) + 2M_1(\varepsilon)R(\phi - \psi_s) + M_0(\varepsilon)R(\phi - \psi_s)^2 \right].
\end{aligned}$$

407 Therefore, the kinetic model (18) in the strong formulation can be approximated
408 (when individuals turn only by a small angle upon interactions with their neigh-
409 bours) by the following Fokker-Planck model **that contains all three social interac-**
410 **tions:**

$$\begin{aligned}
\frac{\partial u}{\partial t} + \gamma e_\phi \cdot \nabla_x u &= \lambda_1 \left(\frac{1}{2\pi} \rho(x, t) - u(x, \phi, t) \right) \\
&+ \frac{\partial}{\partial \phi} \left[-u C^\varepsilon[u, x, \phi] + \frac{\partial}{\partial \phi} (u D^\varepsilon[u, x, \phi]) \right],
\end{aligned} \tag{36}$$

411 with $\lambda_1 = \eta_a + \eta_{al} + \eta_r$ and

$$\begin{aligned}
C^\varepsilon[u, x, \phi] &= C_{al}^\varepsilon[u, x, \phi] + C_r^\varepsilon[u, x, \phi] + C_a^\varepsilon[u, x, \phi], \\
D^\varepsilon[u, x, \phi] &= D_{al}^\varepsilon[u, x, \phi] + D_r^\varepsilon[u, x, \phi] + D_a^\varepsilon[u, x, \phi].
\end{aligned}$$

412 While non-local 2D Fokker-Planck models have been introduced in the past years
413 in connection to self-organised aggregations, the majority of these models consider
414 local diffusion [28, 3]. If we neglect the ε^2 terms (i.e., $B^\varepsilon \approx 0$) and assume $\lambda_1 = 0$,
415 equation (36) reduces to a Vlasov-type flocking equation:

$$\frac{\partial u}{\partial t} + \gamma e_\phi \cdot \nabla_x u + \frac{\partial}{\partial \phi} \left[u C^\varepsilon[u, x, \phi] \right] = 0.$$

416 These type of models have been previously derived from individual-based models
417 (Vicsek or Cucker-Smale models) with or without noise [28, 41, 20].

418 **4. Asymptotic Preserving Methods for 1D models.** The kind of diffusion
419 asymptotics we employed in the previous sections have been numerically investig-
420 ated in [21] using so-called asymptotic preserving (AP) schemes. The AP methods,
421 which improve the scheme already proposed in [39], are a fully explicit variation of
422 the methods introduced in [46, 47]. They are a powerful tool to investigate how
423 patterns are preserved in the parabolic limit by providing numerical schemes for all
424 intermediate models of a scaling process given some scaling parameter $\varepsilon > 0$, and
425 naturally produce a suitable numerical method for the limiting model as $\varepsilon \rightarrow 0$.
426 Here, we apply these schemes only to the 1D models introduced in Section 2, since
427 the numerics become much more complex in two dimensions. Taking advantage of
428 our understanding of the limit process, we base our scheme on a splitting strategy
429 with a convective-like step involving the transport part of the operator and an
430 explicitly solvable ODE step containing stiff sources (see Section 4.2).

4.1. **Odd and Even Parity.** We consider the 1D kinetic model (1) written as an odd-even decomposition,

$$\begin{cases} \partial_t r + \gamma \partial_x j &= 0, \\ \partial_t j + \gamma \partial_x r &= -2\lambda^+[r, j](r + j) + 2\lambda^-[r, j](r - j), \end{cases}$$

with the equilibrium part (macro part/even part) r and the non-equilibrium part (micro part/odd part) j given by

$$r(x, t) = \frac{1}{2} (u^+(x, t) + u^-(x, t)), \quad j(x, t) = \frac{1}{2} (u^+(x, t) - u^-(x, t)).$$

Under scaling assumption (10) for (2), this model reads in the new variables $x = \tilde{x}/\varepsilon, t = \tilde{t}/\varepsilon^2$ as follows:

$$\begin{aligned} \varepsilon \partial_{\tilde{t}} \tilde{r} + \gamma \partial_{\tilde{x}} \tilde{j} &= 0 \\ \varepsilon \partial_{\tilde{t}} \tilde{j} + \gamma \partial_{\tilde{x}} \tilde{r} &= \tilde{r} \lambda_3(f[\tilde{y}^-] - f[\tilde{y}^+]) \\ &\quad - \frac{1}{\varepsilon} \tilde{j} \left(2\lambda_1 + 4\varepsilon \lambda_2 f \left(\tilde{K}^N * \tilde{r} \right) + \varepsilon \lambda_3 (f[\tilde{y}^+] + f[\tilde{y}^-]) \right), \end{aligned}$$

where $\tilde{K}^N(\tilde{x}) = \frac{1}{\varepsilon} K^N(\frac{\tilde{x}}{\varepsilon})$. Rearranging the terms and dropping “ \sim ” for notational convenience, we obtain for r and $J := \frac{1}{\varepsilon} j$:

$$\begin{cases} \partial_t r + \gamma \partial_x J = 0 \\ \partial_t J + \gamma \partial_x r = \frac{1}{\varepsilon^2} r \lambda_3 (f[y^-] - f[y^+]) + \left(1 - \frac{1}{\varepsilon^2} \right) \gamma \partial_x r \\ \quad - \frac{1}{\varepsilon^2} J (2\lambda_1 + 4\varepsilon \lambda_2 f (K^N * r) + \varepsilon \lambda_3 (f[y^+] + f[y^-])). \end{cases} \quad (37)$$

431 4.2. **Operator Splitting.** We can now employ an operator splitting method on
432 (37), separating the stiff source part, which can be treated by an implicit Euler
433 method, and the transport part, which we can solve by an explicit method such as
434 upwinding:

1. **Stiff source part:**

$$\begin{aligned} \partial_t r &= 0, \\ \partial_t J &= \frac{1}{\varepsilon^2} r \lambda_3 (f[y^-] - f[y^+]) + \left(1 - \frac{1}{\varepsilon^2} \right) \gamma \partial_x r \\ &\quad - \frac{1}{\varepsilon^2} J (2\lambda_1 + 4\varepsilon \lambda_2 f (K^N * r) + \varepsilon \lambda_3 (f[y^+] + f[y^-])). \end{aligned} \quad (38)$$

2. **Transport part:**

$$\begin{aligned} \partial_t r + \gamma \partial_x J &= 0, \\ \partial_t J + \gamma \partial_x r &= 0. \end{aligned} \quad (39)$$

435 It can easily be verified that, in the limit $\varepsilon \rightarrow 0$, we recover indeed the macroscopic
436 model (11) for $u = 2r$.

4.3. **Alternated Upwind Discretisation.** In the following, we are interested in the numerical implementation of model (1) with the turning rates (2) depending on a non-linear turning function f without a non-directed density-dependent turning term (i.e. $\lambda_2 = 0$). As shown in Section 2.1, in this case, the parabolic limit yields the drift-diffusion equation (11)

$$\partial_t u = D_0 \partial_{xx} u - B_0 \partial_x (u(f^-[u] - f^+[u])),$$

with $D_0 = \gamma^2/(2\lambda_1)$ and $B_0 = \lambda_3\gamma/(2\lambda_1)$. Note the shortcut notation $f^\pm[u] = f(y_D^\pm[u])$. We propose an alternated upwind discretisation with the even part r evaluated at full grid points $x_i = i\Delta x$, and the odd part J evaluated at half grid points $x_{i+\frac{1}{2}} = (i + \frac{1}{2})\Delta x$. First, we discretise the stiff source part (38) using an implicit Euler discretisation and respecting the direction of the drift. We obtain an explicit expression for J^* ,

$$J_{i+\frac{1}{2}}^* = \frac{\varepsilon^2 J_{i+\frac{1}{2}}^n + \gamma \frac{\Delta t}{\Delta x} (\varepsilon^2 - 1) (r_{i+1}^n - r_i^n)}{\varepsilon^2 + 2\lambda_1 \Delta t + \varepsilon \lambda_3 \Delta t (f^+[r^n] + f^-[r^n])_{i+\frac{1}{2}}} + \frac{\lambda_3 \Delta t \left((f^-[r^n] - f^+[r^n])_{i+\frac{1}{2}}^+ r_i^n + (f^-[r^n] - f^+[r^n])_{i+\frac{1}{2}}^- r_{i+1}^n \right)}{\varepsilon^2 + 2\lambda_1 \Delta t + \varepsilon \lambda_3 \Delta t (f^+[r^n] + f^-[r^n])_{i+\frac{1}{2}}},$$

with $r^* = r^n$. Here, r^n and J^n are the numerical solutions of r and J at time $t_n = n\Delta t$. We use the “*”-notation for half steps in time. Since J is evaluated at half grid point, the discretisation of the transport part (39) can be chosen independently of the sign of the drift,

$$\begin{aligned} \frac{1}{\Delta t} (r_i^{n+1} - r_i^*) + \frac{1}{\Delta x} (J_{i+\frac{1}{2}}^* - J_{i-\frac{1}{2}}^*) &= 0, \\ \frac{1}{\Delta t} (J_{i+\frac{1}{2}}^{n+1} - J_{i+\frac{1}{2}}^*) + \frac{1}{\Delta x} (r_{i+1}^* - r_i^*) &= 0. \end{aligned}$$

Taking the limit $\varepsilon \rightarrow 0$ in the expression for $J_{i+\frac{1}{2}}^*$ and substituting into the first equation of the transport part, we obtain the following discretisation of the one-dimensional macroscopic model (11):

$$\begin{aligned} \frac{u_i^{n+1} - u_i^n}{\Delta t} &= \frac{D_0}{(\Delta x)^2} \left(\partial_{xx}^{(c)} u^n \right)_i \\ &- \frac{B_0}{\Delta x} \left(u_i^n (f^-[r^n] - f^+[r^n])_{i+\frac{1}{2}}^+ - u_{i-1}^n (f^-[r^n] - f^+[r^n])_{i-\frac{1}{2}}^+ \right) \\ &- \frac{B_0}{\Delta x} \left(u_{i+1}^n (f^-[r^n] - f^+[r^n])_{i+\frac{1}{2}}^- - u_i^n (f^-[r^n] - f^+[r^n])_{i-\frac{1}{2}}^- \right). \end{aligned}$$

437 Here, $\partial_{xx}^{(c)} u^n$ denotes the standard central difference discretisations. This illustrates
438 how the choice of discretisation for (38) directly induces a discretisation of model
439 (11). We will now use this scheme to investigate how some of the patterns observed
440 in model (1)-(2) change as $\varepsilon \rightarrow 0$.

441 **Remark 8.** The stability restriction for the proposed AP scheme is less clear. We
442 can expect that the time steps size Δt needs to be sufficiently small, with an upper
443 stability bound depending on the space step size Δx , the diffusion coefficient D_0 ,
444 and the social interaction kernels via the terms $K^N * u$ and $f^\pm[u]$.

445 **4.4. Simulation results.** In Section 2.2 we have seen that for model M4, the two
446 Hopf bifurcations that occurred for the k_4 and k_5 modes have disappeared as $\varepsilon \rightarrow 0$.
447 In this Section, we start with a rotating wave pattern (i.e., travelling pulses) that
448 arises at $\varepsilon = 1$ through a Hopf bifurcation (i.e., for the same parameter values as in
449 Figure 4: $q_a = 1.545$, $q_r = 2.779$, $\lambda_1 = 0.2$, $\lambda_2 = 0$, $\lambda_3 = 0.9$, $\gamma = 0.1$, $A = 2$). Then,
450 we investigate numerically what happens with this pattern as $\varepsilon \rightarrow 0$. The initial
451 conditions for the simulations are random perturbations – of maximum amplitude
452 0.2 – of the spatially homogeneous steady state $u^* = A/2 = 1$. We start with $\varepsilon = 1$,

453 and run the numerical simulations up to $t = 1000$. Then we decrease ε , and choose
 454 the new initial condition to be the final solution obtained with the previous ε value.

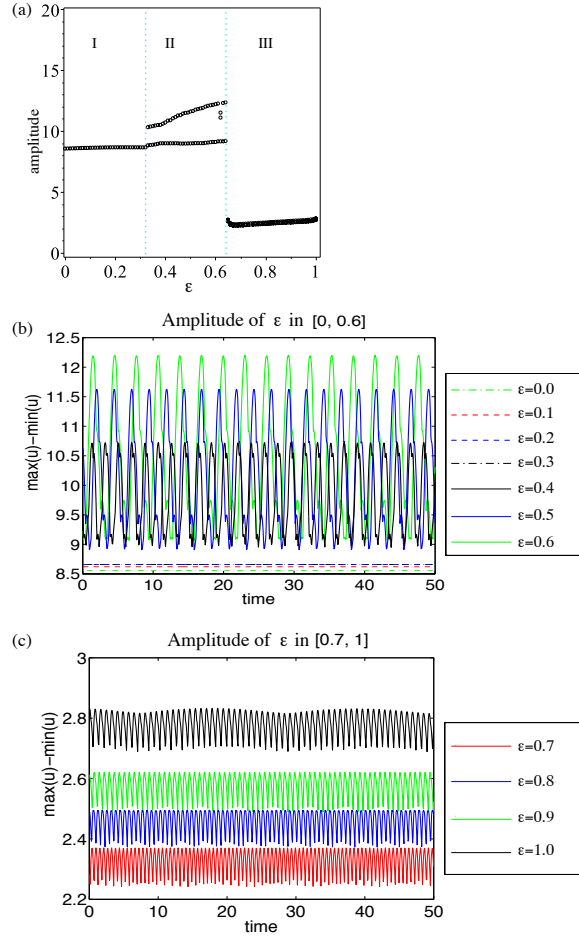


FIGURE 6. The amplitude and density profile of the patterns obtained for $q_a = 1.545$, $q_r = 2.779$, $q_{al} = 0$, $\lambda_1 = 0.2$, $\lambda_2 = 0$, $\lambda_3 = 0.9$ with model M4, as ε is decreased from 1.0 to 0.0. (a) Bifurcation diagram for the amplitude of the patterns as a function of ε . For $\varepsilon \leq 0.32$ (region I), the amplitude is constant. For $\varepsilon \in (0.32, 0.64)$ (region II) the amplitude oscillates between two different values. For $\varepsilon \geq 0.64$ (region III) there are some very small oscillations in the amplitude, however due to the scale of the plot these oscillations are almost unobservable. (b) Amplitude of the patterns for $\varepsilon \in [0, 0.6]$ and for $t \in (0, 50)$. We show here $\max_{x \in [0, L]} u(x, t) - \min_{x \in [0, L]} u(x, t)$, with $u = u^+ + u^-$. (c) Amplitude of the patterns for $\varepsilon \in [0.7, 1.0]$ and for $t \in (0, 50)$.

455 Figure 6(a) shows the amplitude of the patterns obtained when $\varepsilon \in [0, 1]$, for the
 456 particular parameter values mentioned before. Since some of these amplitudes show

457 time-oscillations between different values, we graph their maximum and minimum
 458 values for each ε . As we decrease ε from 1.0 towards 0.64 (region III), the amplitude
 459 undergoes some very small temporal oscillations (see also panel (c)), corresponding
 460 to the rotating wave patterns (with a small time-modulation) shown in Figure 7(c).
 461 For $\varepsilon \in (0.32, 0.64)$ (region II), the amplitude oscillates between two large values.
 462 This corresponds to the “inside-group” zigzagging behaviour shown in Figure 7(b)
 463 near $x = 6$, where the group as a whole does not move in space but individuals
 464 inside the group move between the left and right edges of the group. We also
 465 note a period-doubling bifurcation at $\varepsilon = 0.61$ (region II, Figure 6(a); see the two
 466 dots that appear between the main branches), which leads to a slight decrease
 467 in the amplitude. Finally, as ε is decreased below 0.32 (region I), the movement
 468 inside the group is lost and the pattern is described by stationary pulses with
 469 fixed amplitude (see Figure 6(a) and Figure 7(a)). Figures 6(b),(c) show the time-
 470 variation of the amplitudes of the spatial and spatiotemporal patterns obtained for
 471 $\varepsilon \in [0, 1]$. Figures 7(a’)-(c’) show the density profiles of the patterns observed in
 472 regions I-III.

473 Because the macro-scale models ($\varepsilon = 0$) seem to exhibit stationary pulses (as
 474 shown in Figure 7(a)), we now start with these stationary pulses (for $\varepsilon = 1$) and
 475 investigate whether they change in any way as $\varepsilon \rightarrow 0$. We focus here on model M2
 476 (see Figure 3). Figure 8 shows the amplitude of the stationary pulses obtained with
 477 model M2 in a particular parameter region ($q_a = 2.2$, $q_r = 0.93$, $q_{at} = 0$; see also
 478 Figure 4), as we decrease the scaling parameter ε . We observe that in this case, the
 479 scaling does not affect the patterns or their amplitudes.

480 **Remark 9.** Note that the rotating wave pattern shown in Figure 7(c) for $\varepsilon = 1$
 481 is obtained near a Hopf/steady-state bifurcation (with k_5 the Hopf wavenumber),
 482 and hence the 5 rotating peaks that form this pattern. However, as $\varepsilon \rightarrow 0$, the
 483 wavenumber k_3 seems to become unstable (hence the 3 peaks for the patterns shown
 484 in Figure 7(a),(b)), even if the dispersion relation shown in Figure 4(b) suggests that
 485 k_3 should be stable.

486 **5. Summary and Discussion.** In this study, we investigated the connections
 487 between a class of 1D and 2D non-local kinetic models and their limit macroscopic
 488 models for self-organised biological aggregations. The non-locality of these models
 489 was the result of the assumptions that individuals can interact with neighbours
 490 positioned further away, but still within their perception range. To simplify the
 491 kinetic models that incorporate microscopic-level interactions (such as individuals’
 492 speed and turning rates), we focused on two types of scalings, namely a parabolic
 493 and a grazing collision limit, which lead to parabolic models described in terms of
 494 average speed and average turning behaviour. We showed that while for the kinetic
 495 models the non-local interactions influence the turning rates (i.e., individuals turn
 496 to approach their neighbours, to move away from them or to align with them), for
 497 the limit parabolic models the non-local interactions influence the dispersion and
 498 the drift of the aggregations. In particular, we showed that the assumption that
 499 individuals can turn randomly following the non-directional perception of neigh-
 500 bours around them leads, in the macroscopic scaling, to density-dependent diffu-
 501 sion. Moreover, this diffusion decreased with the increase in the population density.
 502 Biologically, this means that larger animal groups are less likely to spread out.
 503 This phenomenon has been observed for various species. For example, studies have

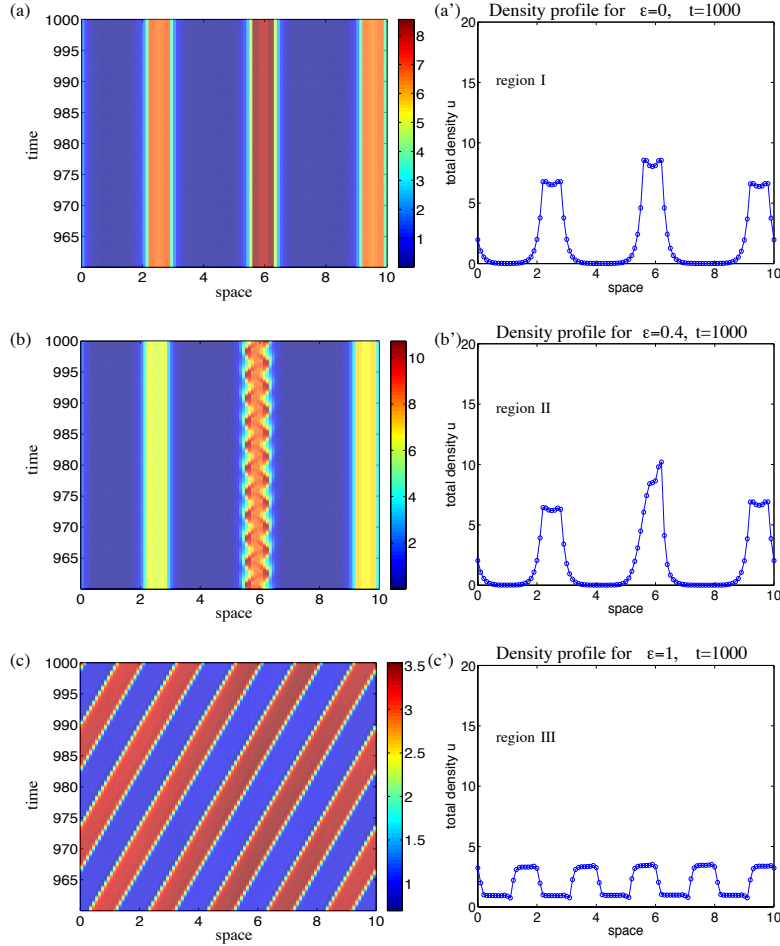


FIGURE 7. The spatial and spatio-temporal patterns obtained with model M4, for $q_a = 1.545$, $q_r = 2.779$, $q_{al} = 0$, $\lambda_1 = 0.2$, $\lambda_2 = 0$, $\lambda_3 = 0.9$, as ε is decreased from 1.0 to 0.0, using model M4. (a) Stationary pulse patterns observed in region I: $\varepsilon \leq 0.32$; (b) "Inside-group" zigzag patterns observed in region II: $\varepsilon \in (0.32, 0.64)$; (c) Rotating wave (traveling pulse) patterns observed in region III: $\varepsilon \geq 0.64$. Panels (a')-(c') show the density profiles corresponding to patterns in panels (a)-(c), at time $t = 1000$.

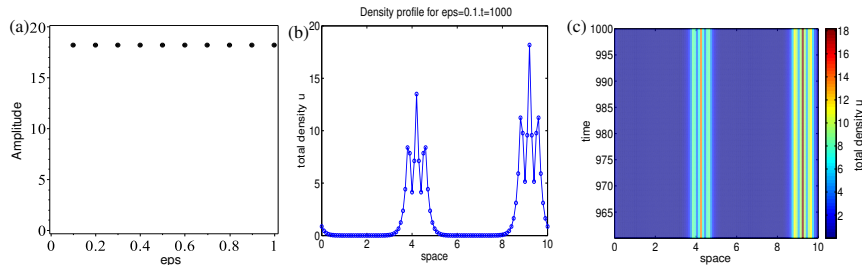


FIGURE 8. The amplitude and density of the patterns obtained for model M2 with $q_a = 2.2$, $q_r = 0.93$, $q_{al} = 0$, $\lambda_1 = 0.2$, $\lambda_2 = 0$, $\lambda_3 = 0.9$, as ε is decreased from 1.0 to 0.0. (a) Bifurcation diagram for the amplitude of the patterns as a function of ε . (b) Density profile for the stationary patterns. (c) Time-space plot of the density.

504 shown that aggregations of locusts [13] or ants [4] can persist only if the number of
 505 individuals is above a certain threshold.

506 The introduction in (2) of the term y_N describing random non-directional turning
 507 (which generalised the turning rates in [33]) was required by the comparison of the
 508 parabolic limit models in 1D and 2D. In particular, the 2D parabolic limit lead to
 509 the natural appearance of this term, which is absent from the 1D parabolic model.
 510 Therefore, to obtain similar parabolic models in 1D and 2D, we had to explicitly add
 511 y_N in equation (2). This suggests that even if the 2D model (18) can be reduced to a
 512 special case of the 1D model (1) (as shown in [36]) there are more subtle differences
 513 between these nonlocal 1D and 2D models. These differences can impact the types
 514 of patterns displayed by the 2D models – an aspect that we will address in a future
 515 study.

516 Next, we investigated how two types of patterns (i.e., travelling and stationary
 517 aggregations) displayed by the 1D kinetic models, were preserved in the limit to
 518 macroscopic parabolic models. To this end, we first investigated the local stabil-
 519 ity of spatially homogeneous patterns characterised by individuals spread evenly
 520 over the domain, and showed that local Hopf bifurcations are lost in the parabolic
 521 limit. These Hopf bifurcations give rise to travelling aggregations (i.e., rotating
 522 waves). We then tested this observation numerically, with the help of asymptotic
 523 preserving methods. We started with a rotating wave pattern obtained near a
 524 Hopf/Steady-state bifurcation for $\varepsilon = 1$ (1D kinetic model; see Figure 7(c)), and
 525 studied numerically how does this pattern change when $\varepsilon \rightarrow 0$ (1D parabolic model;
 526 see Figure 7(a)). By graphing in Figure 6(a) the amplitude of the resulting patterns
 527 as the scaling parameter ε is decreased from $\varepsilon = 1$ to $\varepsilon = 0$, we showed that there
 528 were two major transitions. The first transition occurred around $\varepsilon = 0.64$, when
 529 the travelling (rotating) groups stopped moving. We note, however, that while the
 530 group as a whole was stationary, the individuals inside the group were still mov-
 531 ing between the left- and right-edges of the group, leading to an “inside-group”
 532 zigzagging behaviour. The second transition occurred around $\varepsilon = 0.32$, when the
 533 individuals inside the groups stopped moving, leading to stationary pulses.

534 We emphasise here that this study is one of the first in the literature to investig-
 535 ate numerically the transitions between different aggregation patterns, as a scaling
 536 parameter ε is varied from values corresponding to mesoscale dynamics ($\varepsilon = 1$) to

537 values corresponding to macroscale dynamics ($\varepsilon = 0$). Understanding these trans-
 538 itions is important when investigating biological phenomena that occur on multiple
 539 scales, since it allows us to make decisions regarding the models that are most
 540 suitable to reproduce the observed dynamics.

541 In this study we investigated the preservation of patterns via the 1D parabolic
 542 limit, but similar investigations could be performed for the grazing collision limit.
 543 Moreover, as shown previously [32], model (1) can display many more types of
 544 complex spatio-temporal patterns than the two types of patterns investigated here.
 545 We focused on travelling and stationary aggregations since our aim here was not
 546 to investigate how all possible patterns are preserved by all these different scal-
 547 ing approaches. Rather, it was to show that by taking these asymptotic limits,
 548 some patterns could be lost. Therefore, even if the macroscopic models are sim-
 549 pler to investigate, they might not exhibit the same patterns as the kinetic models.
 550 Our analysis aimed at highlighting the usefulness of asymptotic preserving numer-
 551 ical methods to understand the bifurcation of the solutions as one investigates the
 552 transition from mesoscopic-level to macroscopic-level aggregation dynamics.

553 **Acknowledgments.** JAC, RE and FH acknowledge support from the Engineer-
 554 ing and Physical Sciences Research Council (UK) grants number EP/K008404/1,
 555 EP/K033689/1 and EP/H023348/1 respectively. JAC acknowledges support from
 556 projects MTM2011-27739-C04-02 and the Royal Society through a Wolfson Re-
 557 search Merit Award.

558

References

- 559 [1] E. D. Angelis and B. Lods, On the kinetic theory for active particles: a model for tumor-
 560 immune system competition, *Mathematical and Computer Modeling*, **47** (2008), 196–209.
- 561 [2] A. Arnold, J. A. Carrillo, I. Gamba and C.-w. Shu, Low and high field scaling limits for the
 562 vlasov- and wigner-poisson-fokker-planck systems, *Transp. Theory Stat. Phys.*, **30** (2001),
 563 121–153.
- 564 [3] A. Barbaro and P. Degond, Phase transition and diffusion among socially interacting self-
 565 propelled agents, *Discrete Cont Dyn Syst B. In Press*.
- 566 [4] M. Beekman, D. J. T. Sumpter and F. L. W. Ratnieks, Phase transitions between disordered
 567 and ordered foraging in pharaoh’s ants, *Proc. Natl. Acad. Sci.*, **98** (2001), 9703–9706.
- 568 [5] N. Bellomo, E. D. Angelis and L. Preziosi, Multiscale modeling and mathematical problems
 569 related to tumor evolution and medical therapy, *Journal of Theoretical Medicine*, **5** (2003),
 570 111–136.
- 571 [6] N. Bellomo, A. Bellouquid, J. Nieto and J. Soler, Multicellular biological growing systems:
 572 hyperbolic limits towards macroscopic description, *Mathematical Models and Methods in Ap-
 573 plied Sciences*, **17** (2007), 1675–1693.
- 574 [7] N. Bellomo, C. Bianca and M. Delitala, Complexity analysis and mathematical tools towards
 575 the modelling of living systems, *Physics of Life Reviews*, **6** (2009), 144–175.
- 576 [8] M. G. Bertotti and M. Delitala, Conservation laws and asymptotic behavior of a model of
 577 social dynamics, *Nonlinear Analysis RWA*, **9** (2008), 183–196.
- 578 [9] A. L. Bertozzi, J. A. Carrillo and T. Laurent, Blow-up in multidimensional aggregation equa-
 579 tions with mildly singular interaction kernels, *Nonlinearity*, **22** (2009), 683–710.
- 580 [10] A. Blanchet, J. Dolbeault and B. Perthame, Two-dimensional Keller-Segel model: optimal
 581 critical mass and qualitative properties of the solutions, *Electron. J. Differential Equations*,
 582 No. 44, 32 pp. (electronic).
- 583 [11] M. Bodnar and J. J. L. Velazquez, Derivation of macroscopic equations for individual cell-
 584 based models: a formal approach, *Math. Meth. Appl. Sci.*, **28** (2005), 1757–1779.
- 585 [12] R. Breitwisch and G. Whitesides, Directionality of singing and non-singing behaviour of mated
 586 and unmated Northern Mockingbirds, *Mimus polyglottos*, *Anim. Behav.*, **35** (1987), 331–339.
- 587 [13] J. Buhl, D. J. T. Sumpter, I. D. Couzin, J. J. Hale, E. Despland, E. R. Miller and S. J.
 588 Simpson, From disorder to order in marching locusts, *Science*, **312** (2006), 1402–1406.

- 589 [14] P.-L. Buono and R. Eftimie, Analysis of Hopf/Hopf bifurcations in nonlocal hyperbolic models
590 for self-organised aggregations, *Math. Models Methods Appl. Sci.*, **24** (2014), 327.
- 591 [15] P.-L. Buono and R. Eftimie, Codimension-two bifurcations in animal aggregation models with
592 symmetry, *SIAM J. Appl. Dyn. Syst.*
- 593 [16] P.-L. Buono and R. Eftimie, Symmetries and pattern formation in hyperbolic versus parabolic
594 models for self-organised aggregations, *J. Math. Biol.*
- 595 [17] M. Burger, V. Capasso and D. Morale, On an aggregation model with long and short range
596 interactions, *Nonlinear Analysis: Real World Applications*, **8** (2007), 939–958.
- 597 [18] J. A. Carrillo, M. R. D’Orsogna and V. Panferov, Double milling in self-propelled swarms
598 from kinetic theory, *Kinetic and Related Models*, **2** (2009), 363–378.
- 599 [19] J. A. Carrillo, M. Fornasier, J. Rosado and G. Toscani, Asymptotic flocking dynamics for the
600 kinetic Cucker-Smale model, *SIAM J. Math. Anal.*, **42** (2010), 218–236.
- 601 [20] J. A. Carrillo, M. Fornasier, G. Toscani and F. Vecil, Particle, kinetic, and hydrodynamic
602 models of swarming, *Mathematical Modelling of Collective Behavior in Socio-Economic and*
603 *Life Sciences*, 297–336.
- 604 [21] J. A. Carrillo, T. Goudon, P. Lafitte and F. Vecil, Numerical schemes of diffusion asymptotics
605 and moment closures for kinetic equations, *J. Sci. Comput.*, **36** (2008), 113–149, URL <http://dx.doi.org/10.1007/s10915-007-9181-5>.
- 606 [22] J. A. Carrillo, Y. Huang and S. Martin, Explicit flock solutions for quasi-morse potentials, *to*
607 *appear in European Journal of Applied Mathematics*.
- 608 [23] J. A. Carrillo, A. Klar, S. Martin and S. Tiwari, Self-propelled interacting particle systems
609 with roosting force, *Math. Models Methods Appl. Sci.*, **20** (2010), 1533.
- 610 [24] J. A. Carrillo and B. Yan, An asymptotic preserving scheme for the diffusive limit of kinetic
611 systems for chemotaxis, *Multiscale Model. Simul.*, **11** (2013), 336–361, URL <http://dx.doi.org/10.1137/110851687>.
- 612 [25] A. Chertock, A. Kurganov, A. Polizzi and I. Timofeyev, Pedestrian flow models with slowdown
613 interactions, *Math Models Methods Appl. Sci.*, **24** (2014), 249–275.
- 614 [26] Y.-L. Chuang, M. R. D’Orsogna, D. Marthaler, A. L. Bertozzi and L. S. Chayes, State transi-
615 tions and the continuum limit for a 2d interactiong, self-propelled particle system, *Physica D*,
616 **232** (2007), 33–47.
- 617 [27] P. Degond, G. Dimarco and T. Mac, Hydrodynamics of the Kuramoto-Vicsek model of ro-
618 tating self-propelled particles, *Mathematical Models and Methods in Applied Sciences*, **24**
619 (2014), 277–325.
- 620 [28] P. Degond and S. Motsch, Macroscopic limit of self-driven particles with orientation interac-
621 tion, *C.R. Acad. Sci. Paris Ser. I*, **345** (2007), 555–560.
- 622 [29] P. Degond and S. Motsch, Large scale dynamics of the persistent turning awlker model of fish
623 behaviour, *J. Stat. Phys.*, **131** (2008), 989–1021.
- 624 [30] R. Eftimie, *Modeling group formation and activity patterns in self-organizing communities*
625 *of organisms*, PhD thesis, University of Alberta, 2008.
- 626 [31] R. Eftimie, Hyperbolic and kinetic models for self-organized biological aggregations and move-
627 ment: a brief review, *J. Math. Biol.*, **65** (2012), 35–75.
- 628 [32] R. Eftimie, G. de Vries and M. A. Lewis, Complex spatial group patterns result from different
629 animal communication mechanisms, *Proc. Natl. Acad. Sci.*, **104** (2007), 6974–6979.
- 630 [33] R. Eftimie, G. de Vries, M. A. Lewis and F. Lutscher, Modeling group formation and activity
631 patterns in self-organizing collectives of individuals, *Bull. Math. Biol.*, **69** (2007), 1537–1566.
- 632 [34] R. Eftimie, G. de Vries and M. Lewis, Weakly nonlinear analysis of a hyperbolic model for
633 animal group formation, *J. Math. Biol.*, **59** (2009), 37–74.
- 634 [35] R. Eftimie and U. of Alberta (Canada)., *Modeling Group Formation and Activity Patterns in*
635 *Self-organizing Communities of Organisms*, Canadian theses, University of Alberta (Canada),
636 2008, URL <http://books.google.co.uk/books?id=YKSsnBUzYToC>.
- 637 [36] R. Fetecau, Collective behavior of biological aggregations in two dimensions: a nonlocal kinetic
638 model, *Math. Model. Method. Appl. Sci.*, **21** (2011), 1539.
- 639 [37] E. Geigant, K. Ladizhansky and A. Mogilner, An integrodifferential model for orientational
640 distributions of F-actin in cells, *SIAM J. Appl. Math.*, **59** (1998), 787–809.
- 641 [38] E. Geigant, K. Ladizhansky and A. Mogilner, An integrodifferential model for orientational
642 distributions of F-actin in cells, *SIAM J. Appl. Math.*, **59** (1999), 787–809 (electronic).
- 643 [39] P. Godillon-Lafitte and T. Goudon, A coupled model for radiative transfer: Doppler effects,
644 equilibrium, and nonequilibrium diffusion asymptotics, *Multiscale Model. Simul.*, **4** (2005),
645 1245–1279, URL <http://dx.doi.org/10.1137/040621041>.
- 646
- 647

- 648 [40] T. Goudon, On Boltzmann equations and Fokker-Plank asymptotics: influence of grazing
649 collisions, *J. Stat. Phys.*, **89** (1997), 751–776.
- 650 [41] S.-Y. Ha and E. Tadmor, From particle to kinetic and hydrodynamic descriptions of flocking,
651 *Kinetic and Related Models*, **1** (2008), 415–435.
- 652 [42] C. K. Hemelrijk and H. Kunz, Density distribution and size sorting in fish schools: an
653 individual-based model, *Behav. Ecol.*, **16** (2004), 178–187.
- 654 [43] H. Hildenbrandt, C. Carere and C. K. Hemelrijk, Self-organised complex aerial displays of
655 thousands of starlings: a model, *Behavioral Ecology*, **107** (2010), 1349–1359.
- 656 [44] T. Hillen and H. G. Othmer, The diffusion limit of transport equations derived from velocity
657 jump process, *SIAM J. Appl. Math.*, **61** (2000), 751–775.
- 658 [45] E. E. Holmes, Are diffusion models too simple? A comparison with telegraph models of
659 invasion, *Am. Nat.*, **142** (1993), 779–795.
- 660 [46] A. Klar, An asymptotic-induced scheme for nonstationary transport equations in the diffusive
661 limit, *SIAM J. Numer. Anal.*, **35** (1998), 1073–1094 (electronic), URL [http://dx.doi.org/
662 10.1137/S0036142996305558](http://dx.doi.org/10.1137/S0036142996305558).
- 663 [47] A. Klar, An asymptotic preserving numerical scheme for kinetic equations in the low Mach
664 number limit, *SIAM J. Numer. Anal.*, **36** (1999), 1507–1527 (electronic), URL [http://dx.
665 doi.org/10.1137/S0036142997321765](http://dx.doi.org/10.1137/S0036142997321765).
- 666 [48] R. Larkin and R. Szafoni, Evidence for widely dispersed birds migrating together at night,
667 *Integrative and comparative biology*, **48** (2008), 40–49.
- 668 [49] A. Mogilner and L. Edelstein-Keshet, A non-local model for a swarm, *J. Math. Biol.*, **38**
669 (1999), 534–570.
- 670 [50] A. Mogilner and L. Edelstein-Keshet, A non-local model for a swarm, *J. Math. Biol.*, **38**
671 (1999), 534–570, URL <http://dx.doi.org/10.1007/s002850050158>.
- 672 [51] A. Mogilner, L. Edelstein-Keshet and G. B. Ermentrout, Selecting a common direction. II.
673 Peak-like solutions representing total alignment of cell clusters, *J. Math. Biol.*, **34** (1996),
674 811–842.
- 675 [52] D. Morale, V. Capasso and K. Oelschläger, An interacting particle system modelling ag-
676 gregation behavior: from individuals to populations, *J. Math. Biol.*, **50** (2005), 49–66, URL
677 <http://dx.doi.org/10.1007/s00285-004-0279-1>.
- 678 [53] I. Newton, *The migration ecology of birds*, Academic Press, Elsevier, 2008.
- 679 [54] H. G. Othmer and T. Hillen, The diffusion limit of transport equations II: chemotaxis equa-
680 tions, *SIAM J. Appl. Math.*, **62** (2002), 1222–1250.
- 681 [55] R. D. Passo and P. de Mottoni, Aggregative effects for a reaction-advection equation, *J. Math.*
682 *Biology*, **20** (1984), 103–112.
- 683 [56] B. Pfister, A one dimensional model for the swarming behaviour of Myxobacteria, in *Biolo-*
684 *gical Motion, Lecture Notes on Biomathematics*, 89 (eds. W. Alt and G. Hoffmann), Springer,
685 1990, 556–563.
- 686 [57] J. Saragosti, V. Calvez, N. Bournaveas, A. Buguin and P. S. B. Perthame, Mathematical
687 description of bacterial traveling pulses, *PLOS Computational Biology*, **6** (2010), e1000890.
- 688 [58] J. Saragosti, V. Calvez, N. Bournaveas, A. Buguin, P. Silberzan and B. Perthame, Mathem-
689 atical description of bacterial traveling pulses, *PLoS Comput. Biol.*, **6** (2010), e1000890, 12,
690 URL <http://dx.doi.org/10.1371/journal.pcbi.1000890>.
- 691 [59] C. M. Topaz, A. L. Bertozzi and M. A. Lewis, A nonlocal continuum model for biological
692 aggregation, *Bull. Math. Bio.*, **68** (2006), 1601–1623.
- 693 [60] F. Venuti, L. Bruno and N. Bellomo, Crowd dynamics on a moving platform: mathematical
694 modelling and application to lively footbridges, *Mathematical and Computer Modelling*, **45**
695 (2007), 252–269.

696 Received xxxx 20xx; revised xxxx 20xx.

697 *E-mail address:* carrillo@imperial.ac.uk

698 *E-mail address:* reftimie@maths.dundee.ac.uk

699 *E-mail address:* fkoh2@cam.ac.uk